The Impact of Topography and Eddy Parameterization on the Simulated Southern Ocean Circulation Response to Changes in Surface Wind Stress

HAILU KONG^a AND MALTE F. JANSEN^a

^a Department of the Geophysical Sciences, University of Chicago, Chicago, Illinois

(Manuscript received 24 June 2020, in final form 8 December 2020)

ABSTRACT: It remains uncertain how the Southern Ocean circulation responds to changes in surface wind stress, and whether coarse-resolution simulations, where mesoscale eddy fluxes are parameterized, can adequately capture the response. We address this problem using two idealized model setups mimicking the Southern Ocean: a flat-bottom channel and a channel with moderately complex topography. Under each topographic configuration and varying wind stress, we compare several coarse-resolution simulations, configured with different eddy parameterizations, against an eddy-resolving simulation. We find that 1) without topography, sensitivity of the Antarctic Circumpolar Current (ACC) to wind stress is overestimated by coarse-resolution simulations, due to an underestimate of the sensitivity of the eddy diffusivity; 2) in the presence of topography, stationary eddies dominate over transient eddies in counteracting the direct response of the ACC and overturning circulation to wind stress changes; and 3) coarse-resolution simulations with parameterized eddies capture this counteracting effect reasonably well, largely due to their ability to resolve stationary eddies. Our results highlight the importance of topography in modulating the response of the Southern Ocean circulation to changes in surface wind stress. The interaction between mesoscale eddies and stationary meanders induced by topography requires more attention in future development and testing of eddy parameterizations.

KEYWORDS: Southern Ocean; Eddies; Meridional overturning circulation; Ocean models; Parameterization

1. Introduction

The Southern Ocean plays a crucial role in Earth's climate and global ocean dynamics. It connects major ocean basins through its Antarctic Circumpolar Current (ACC) and the associated meridional overturning circulation (MOC). Both of these components are fundamentally driven by surface wind stress, which has been increasing for decades and is projected to further increase in the future (e.g., Swart and Fyfe 2012). An important question therefore is how the ACC and MOC respond to changes in surface wind stress.

Straub (1993) proposes that the baroclinic ACC transport may remain steady despite the changes in surface wind stress, due to the role of mesoscale eddies in adjusting the isopycnal structure, a scenario that has been called "eddy saturation." An increase in surface wind stress steepens the isopycnals, which increases the baroclinic ACC transport (following the thermal wind relation), builds up available potential energy, and enhances baroclinic instability. Consequently, mesoscale eddies strengthen and tend to flatten the isopycnals, which weakens the ACC transport response. In fact, Böning et al. (2008) found no evidence of ACC transport change so far, despite significant surface wind stress increase during the past decades.

Mesoscale eddies are also crucial in the maintenance of the Southern Ocean MOC by generating an eddy-induced MOC that flattens the isopycnals and counteracts the wind-driven MOC. Hallberg and Gnanadesikan (2006) propose that when wind stress increases, the eddy-induced MOC will adjust so as

Corresponding author: Hailu Kong, hlkong@uchicago.edu

to compensate for the increase in the wind-driven MOC, resulting in an insensitive residual MOC, an effect that has been called "eddy compensation" (Viebahn and Eden 2010).

The key ingredient to both the eddy saturation and compensation arguments are mesoscale eddies, which, due to their small size, have to be parameterized in most comprehensive general circulation models (GCMs). The effect of mesoscale eddies on the density field is typically parameterized via the Gent and McWilliams (1990, hereafter GM) parameterization, which induces an eddy-driven overturning proportional to the isopycnal slope times the GM "diffusivity." However, models differ significantly in their choices for the GM diffusivity, which can itself be a function of the mean flow. Previous studies have shown that the ACC and MOC response to wind stress changes in ocean and climate models is often sensitive to the choice of GM diffusivity (e.g., Farneti et al. 2010; Farneti and Gent 2011; Kuhlbrodt et al. 2012; Farneti et al. 2015; Poulsen et al. 2018). Farneti et al. (2015) compare simulations of 1958–2007 climate across a number of ocean GCMs configured with different eddy parameterizations or at eddy-permitting resolutions. They find that the degree of eddy saturation is almost perfect in all models; by contrast, the degree of eddy compensation diverges significantly across the GCMs. Specifically, they find that the degree of eddy compensation tends to be higher in the models that either use an eddy-permitting resolution without eddy parameterizations, or adopt a 3D spatial structure for the GM diffusivity, while the degree of eddy compensation is lower in the models that employ only a 2D or 1D spatial structure for the GM diffusivity. Poulsen et al. (2018) compare the transient response of the MOC to wind stress changes in two configurations of the same GCM, one with fully resolved mesoscale eddies and the other with parameterized eddies. They find that

the MOC in the two configurations responds similarly to decreased wind stress but significantly differently to increased wind stress. Complex GCM simulations hence tend to suggest that eddy compensation is more pronounced in high-resolution simulations or those with sophisticated eddy parameterizations. However, the results are not always consistent and interpretation is challenging due to the general complexity of the models, the potential sensitivity on simulation time and initial conditions (Sinha and Abernathey 2016; Jansen et al. 2018), and the fact that different models typically differ in many aspects other than their representation of mesoscale eddies. Unfortunately, direct observation of the residual MOC remains challenging (e.g., Rintoul and Naveira Garabato 2013), making it difficult to conclude which GCM yields the best estimate of the MOC.

Idealized models have therefore played an important role for both testing eddy parameterizations and improving mechanistic understanding (Hallberg and Gnanadesikan 2006; Viebahn and Eden 2010; Abernathey et al. 2011; Allison et al. 2011; Munday et al. 2013; Morrison and Hogg 2013; Abernathey and Cessi 2014; Nadeau and Ferrari 2015; Mak et al. 2018; Constantinou 2018; Constantinou and Hogg 2019). Yet, only a few studies have compared the degree of eddy saturation and/or compensation in non-eddying simulations with state-of-the-art eddy parameterizations, against an eddy-resolving simulation in the same model configuration. Mak et al. (2018) find almost perfect eddy saturation in an idealized eddy-permitting model of the Southern Ocean. They show that coarse-resolution simulations using their new Geometry and Energetics of Ocean Mesoscale Eddies and Their Rectified Impact on Climate (GEOMETRIC) parameterization can reproduce this result, while simulations with a constant GM diffusivity fail to adequately capture the eddy saturation. By contrast, their coarse-resolution simulations using GEOMETRIC or a constant GM diffusivity can both produce a similar degree of eddy compensation as in the eddy-permitting simulation. Viebahn and Eden (2010) instead find that coarseresolution simulations with eddy parameterizations predict a lower degree of eddy compensation than an eddy-permitting simulation. One difference between the two studies is the topography: while both studies use a model that has a reentrant channel connected to a basin in the north, the channel region in Viebahn and Eden (2010) has a flat bottom, while the model of Mak et al. (2018) includes a meridional ridge in the channel area, which blocks bottom zonal flow and generates stationary meanders.

Topography plays a crucial role in the Southern Ocean circulation. It generates significant bottom form stress that dominantly balances the zonal momentum imparted by surface wind stress, thereby closing the barotropic zonal momentum budget (Munk and Palmén 1951). Above the height of the topography, stationary meanders add to the effect of the transient eddies in transferring the zonal momentum downward via internal form stress (Johnson and Bryden 1989). Topography also generates local hotspots of eddy kinetic energy (EKE), which are collocated with flattened isopycnals (Thompson and Naveira Garabato 2014). Topography has been shown to suppress the response of the baroclinic ACC transport to wind stress changes through enhancing local buoyancy gradients and elongating buoyancy contours across which the eddies transport buoyancy meridionally, thus

transferring momentum downward (Abernathey and Cessi 2014). While the effect of topography on ACC transport has thus received significant attention, the effect on the MOC, and especially eddy compensation, has not been systematically explored, although some studies have touched on this topic (e.g., Wang et al. 2016).

In this work we use an idealized model setup to investigate the influence of topography on both baroclinic eddy saturation and compensation, and examine in how far these processes can be reproduced in coarse-resolution simulations with state-of-the-art eddy parameterizations. We show that topography significantly amplifies the degree of both eddy compensation and saturation, leading to relatively insensitive MOC and ACC transport. Moreover, the ACC and MOC responses to wind stress changes are reasonably well captured by coarse-resolution simulations with a range of different eddy parameterizations if, and only if, topography is present.

2. Model configuration

We perform our experiments using an isopycnal configuration of the GFDL Modular Ocean Model 6 (MOM6), with 30 isopycnal layers. We employ two different topographic configurations, shown in Fig. 1. Both configurations share the same domain size, spanning from 65° to 30°S in latitude and covering 60° in longitude with periodic zonal boundary conditions. The longitudinal extent is chosen to minimize computational expense while still allowing for substantial stationary meanders associated with large topography. The flat-bottom configuration (left panel) is a zonally reentrant channel, similar to the one used by Abernathey et al. (2011), but with a continental slope along Antarctica. The full topography configuration (right panel) has a meridional continental barrier (mimicking Patagonia) and a subsurface ridge encircling Drake Passage (mimicking Scotia Arc). Drake Passage is the only reentrant part, which opens between 61° and 53°S at the surface and becomes slightly narrower at depth. We have also included a topographic slope along the southern, eastern, and western boundaries, as well as along Scotia Arc. Away from the topographic features, the sea floor is 4 km deep, and Scotia Arc rises to a depth of 2.5 km.

We use two horizontal resolutions: 0.1° for the eddy-resolving simulations, and 1° for the non-eddying simulations where eddy parameterizations are used. The model adopts a Mercator grid so its latitudinal grid spacing (in physical distance) roughly matches that of its longitudinal grid spacing. The aforementioned resolutions refer to the longitudinal increment. The latitudinal increment decreases poleward to maintain roughly square grid boxes.

The model is forced with zonally symmetric wind stress that peaks at 53°S and vanishes at the southern and northern boundaries (Fig. 2a):

$$\tau(\theta) = \begin{cases} \tau_0 \cos\left[\frac{15}{2}(\theta + 53^\circ)\right], & \theta \le -53^\circ, \\ \frac{1}{2}\tau_0 \left\{1 + \cos\left[\frac{36}{5}(\theta + 53^\circ)\right]\right\}, & \theta > -53^\circ, \end{cases}$$
(1)

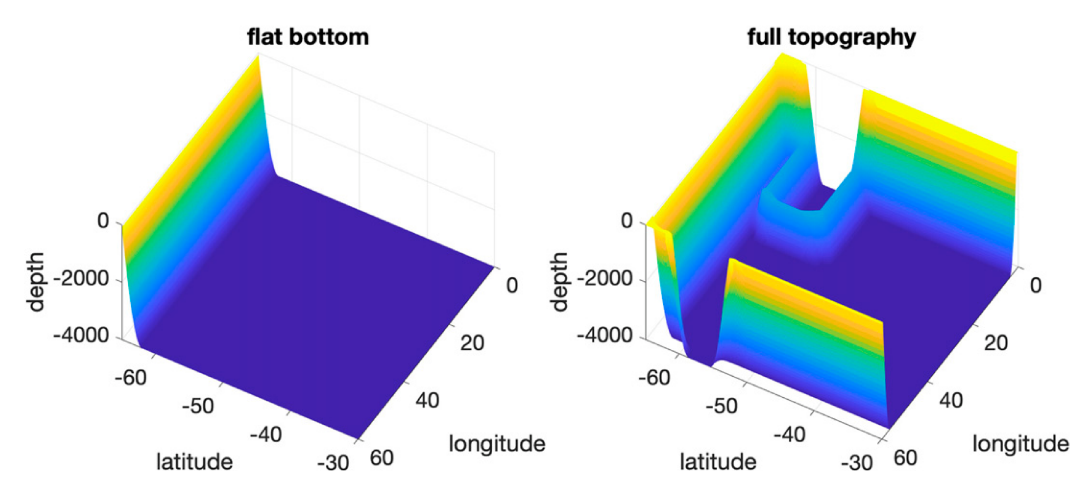


FIG. 1. The two topography configurations used in this study, with color shading denoting the depth. A no-flux condition is applied at the northern boundary. A 1° -wide sponge layer is applied to restore the buoyancy profile at the northern end in the simulations used to study the MOC.

where θ is latitude, $\tau_0 = 0.2 \,\text{Pa}$ is the peak wind stress in the reference case, and $\tau_0 = 0, 0.05, 0.1$, and 0.3 Pa in the wind stress sensitivity experiments.

The model's surface potential density is restored toward a target density profile (Fig. 2b), with a piston velocity of 2 m day^{-1} :

$$\sigma_2(\theta) = 1031.30 - 0.0954\theta \ . \tag{2}$$

We employ two types of buoyancy boundary conditions at the northern end of the domain to explore the responses of the MOC and ACC transport to wind stress changes. To investigate the response of the MOC, we use a "sponge layer" at the northern boundary, which represents the diabatic transformation of water masses taking place in the basin to the north of the Southern Ocean in the real world (Abernathey et al. 2011; Morrison and Hogg 2013). In the sponge layer, vertical stratification is restored toward a prescribed profile, shown in Fig. 2c. The sponge layer is 1° wide latitudinally. The restoring rate is $(7 \text{ day})^{-1}$ at the very boundary and decreases linearly toward the southern edge of the sponge layer where it becomes 0. The sponge layer enables us to investigate the response of the MOC to changes in surface wind stress with the channel configuration because it allows for a nontrivial residual MOC. However, the sponge layer is not suitable to investigate the response of the ACC transport, because, together with the surface restoring condition, the two boundary conditions specify the baroclinicity in the channel to a level where there is very little room for the ACC transport to adjust. In other words, the sponge layer allows us to investigate eddy compensation in a limit where eddy saturation is essentially enforced.

To investigate the response of the ACC transport, we adopt an adiabatic boundary condition [i.e., no sponge layer; as, e.g., in Abernathey and Cessi (2014)]. This allows isopycnals to freely evolve so that changes in the ACC transport in response to varying surface wind stress can be represented. By construction, this setup does not allow any nontrivial MOC to exist (except for that induced by diapycnal mixing within the Southern Ocean), and is therefore not suitable to investigate the MOC's response to wind stress changes. This setup can be used to explore eddy saturation in the limit of approximate eddy compensation. We summarize key model parameters in Table 1. All simulations have been integrated to a statistically steady state, for at least 200 model years.

3. Eddy parameterizations

The eddy parameterizations we test in this work are all based on the GM framework (Gent and McWilliams 1990; Gent et al. 1995). The GM framework parameterizes the eddy-induced streamfunction as

$$\psi_{\rm GM} = \mathbf{k} \times \kappa_{\rm GM} \mathbf{s},\tag{3}$$

where **k** is the vertical unit vector, κ_{GM} is the GM diffusivity, and $\mathbf{s} = \nabla_{\sigma} z$ is the isopycnal slope (the subscript σ denotes that the gradient is taken along an isopycnal; Vallis 2006). The parameterized overturning circulation ψ_{GM} flattens the isopycnals that are tilted by the wind-driven Ekman transport, and hence releases available potential energy from the resolved flow. Notice that the GM parameterization represents the advective effect of eddies, which makes the interpretation of κ_{GM} as an eddy "diffusivity" questionable. However, for small isopycnal slopes (a good assumption outside of the mixed layer), κ_{GM} relates the horizontal component of the eddy buoyancy flux to the mean horizontal buoyancy gradient (e.g., Plumb and Ferrari 2005). We therefore here adopt the

 $^{^1}$ This profile has been determined by running an extended version of the model (with full topography) which includes an interhemispheric basin with northern deep water formation to the north of the channel. This extended version of the model was run at 1° resolution with a simple eddy parameterization that has a constant GM diffusivity of $700\,\mathrm{m}^2\,\mathrm{s}^{-1}$. The detailed structure of the sponge layer does not alter the conclusions of this work.

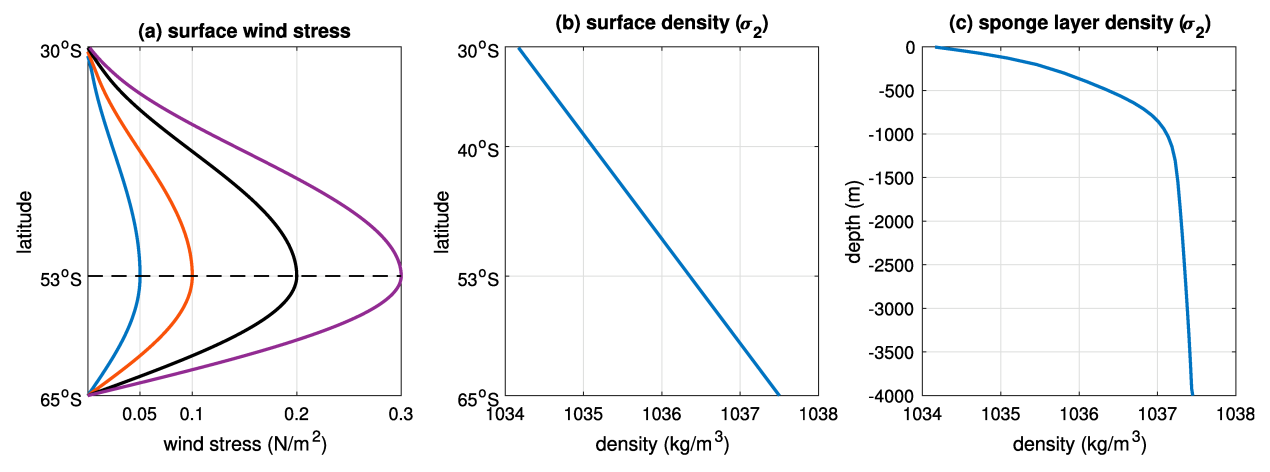


FIG. 2. The model's boundary conditions. (a) Surface zonal wind stress profile, (b) the target surface potential density profile, and (c) the target potential density profile toward which buoyancy is restored in the sponge layer (where applied, see text).

common interpretation of κ_{GM} as a horizontal eddy buoyancy diffusivity, although we note that, in the ocean interior, a vertical eddy flux component that aligns the buoyancy flux along the isopycnal slope is implied.

The eddy parameterizations we test in this work vary only in their formulations of the GM diffusivity. The first suite of simulations use a constant GM diffusivity: 0, 100, 200, ..., 700 m² s⁻¹. The second eddy parameterization we test is based on Visbeck et al. (1997) and computes the GM diffusivity based on the local baroclinicity and stratification. The third eddy parameterization is based on Jansen et al. (2015) and computes the GM diffusivity based on a prognostic equation for the mesoscale eddy kinetic energy (MEKE; see also Eden and Greatbatch 2008). The last eddy parameterization is a modified version of the MEKE parameterization that considers the suppression of the GM diffusivity by the topographic β effect, and therefore is named TMEKE ("T" for topographic; see also Jansen et al. 2019). The GM diffusivity in the Visbeck, MEKE, and TMEKE eddy parameterizations varies temporarily and horizontally but not vertically. Although the MEKE and TMEKE parameterizations generally have multiple parameters we here only tune one parameter for each of these three eddy parameterizations, to qualitatively match the high-resolution simulation results as accurately as possible (see appendix A for additional details and parameter values). We have also tested vertically varying GM diffusivities, either through imposing an equivalent barotropic structure to the GM diffusivity, or by solving a vertical elliptic equation for the eddy-induced streamfunction (Ferrari et al. 2010). However, we have found that including a vertical structure in the eddy parameterization does not improve our results, and have thus not included it in the eddy parameterizations discussed in this paper. The acronyms for the various eddy parameterizations are listed in Table 2, and additional details are provided in appendix A.

4. Results

We compare different eddy parameterizations by running the same model configurations with two resolutions: a 0.1° eddy-resolving simulation, and several 1° non-eddying simulations with different eddy parameterizations. We first consider the reference setup, where we include the full topography and force the model with present-day wind stress ($\tau_0 = 0.2$ Pa), with and without the sponge layer at the northern boundary. The setup with the sponge layer is used to investigate the MOC, while the one without the sponge layer is used to investigate the ACC transport. We then vary wind stress to test how the eddy parameterizations capture the response of the ACC transport and the MOC to wind stress changes under different topography and using different eddy parameterizations.

a. Performance of eddy parameterizations in the reference setup

In this part we test the eddy parameterizations' ability to reproduce high-resolution simulations in the reference case with full topography and wind stress $\tau_0 = 0.2$ Pa. Three metrics are used to evaluate the eddy parameterizations: 1) the baroclinic ACC transport in the simulations with an adiabatic northern boundary condition, 2) the MOC in the simulations with a sponge layer at the northern boundary, and 3) the isopycnal interface height error ϵ in both configurations. We find that the simulations using variable GM diffusivities generally better reproduce the ACC transport, the MOC, and the isopycnal height field of the high-resolution reference simulations, with the energy-budget-based parameterization with topographic β effect (TMEKE) performing best overall.

TABLE 1. Key model parameters.

Parameter	Value
Piston velocity for surface density restoring	$2 \mathrm{m} \mathrm{day}^{-1}$
Maximum sponge layer restoring rate	$(7 \text{ day})^{-1}$ $0.05 \text{ m s}^{-1} \times \Delta^3$
Biharmonic viscosity	$0.05 \mathrm{ms}^{-1} \times \Delta^3$ (Δ is grid spacing)
Diapycnal diffusivity	$5 \times 10^{-5} \mathrm{m}^2 \mathrm{s}^{-1}$
Quadratic bottom drag coefficient	0.003

TABLE 2. Acronyms for eddy parameterizations (see appendix A for a detailed description).

Acronym	Eddy parameterization
$\kappa_7, \kappa_6, \ldots, \kappa_0$	Constant GM diffusivity: 700, 600,, 0 ($m^2 s^{-1}$)
Visbeck	Based on Visbeck et al. (1997)
MEKE	Mesoscale eddy kinetic energy (Jansen et al. 2015)
TMEKE	Topographic MEKE (Jansen et al. 2019)

1) BAROCLINIC ACC TRANSPORT

We focus on the baroclinic component of the ACC transport, which is computed as the total zonally averaged ACC transport minus the transport associated with the bottom geostrophic flow:

$$T_{\rm ACC} = \iint [\overline{u}_{\rm bc}] \, dy \, dz = \iiint \left[\overline{u} + \frac{1}{f\rho_0} \, \partial_y \overline{p}(z_{\rm bot}) \right] \, dy \, dz \,, \qquad (4)$$

where $[\cdot]$ denotes a zonal average, $\overline{(\cdot)}$ denotes a temporal average (over 20 years in the 0.1° simulations and 50 years in the 1° simulations), u_{bc} is the baroclinic zonal velocity, u is the full zonal velocity, f is the Coriolis parameter, f is the reference density, and f is the hydrostatic pressure gradient at the sea floor (with the meridional derivative taken at fixed depth).

We find that the baroclinic ACC transport can be well reproduced in the coarse-resolution simulations with either a variable GM diffusivity or a constant GM diffusivity $\kappa_{\rm GM} \sim 400\,{\rm m}^2\,{\rm s}^{-1}$, as is shown in Fig. 3. When a constant GM diffusivity is adopted, the qualitative relation between the diffusivity and the ACC transport is as expected: because the GM diffusivity works to flatten the isopycnal slope, a larger GM diffusivity leads to smaller isopycnal slopes, which in turn results in a weaker baroclinic ACC transport.

2) MOC

Next we compare the MOC across the simulations employing a northern sponge layer. The MOC in the 0.1° simulation is computed as

$$\psi(y,\sigma) = \oint_{x} \int_{\sigma}^{\sigma} \overline{v(x,y,\hat{\sigma}) \cdot h(x,y,\hat{\sigma})} \, d\hat{\sigma} \, dx. \tag{5}$$

where σ_s is the surface density and $h = -\partial z/\partial \sigma$ is the isopycnal layer thickness (h = 0 on isopycnals that vanish due to inoutcropping). In the 1° simulations the MOC is computed as

$$\psi(y,\sigma) = \oint_{x} \int_{\sigma_{c}}^{\sigma} \overline{v(x,y,\hat{\sigma}) \cdot h(x,y,\hat{\sigma}) + vh_{GM}(x,y,\hat{\sigma})} \, d\hat{\sigma} \, dx, \quad (6)$$

where $vh_{GM}=\partial\psi_{GM}^{\gamma}/\partial\sigma$ is the parameterized eddy thickness flux. The magnitude of the upper MOC cell is defined as the maximum of ψ along the $\sigma=1037$ kg m⁻³ isopycnal, where the center of the upper cell resides in the high-resolution simulation. The magnitude of the lower cell is defined as the minimum of

 ψ along the $\sigma = 1037.42 \, \text{kg m}^{-3}$ isopycnal. The main results in this work are insensitive to where exactly the MOC is evaluated.

We find that the upper MOC cell is relatively well represented with either variable GM diffusivities or a small constant GM diffusivity, as is shown in Fig. 4. By contrast, the lower cell is generally less well represented in the non-eddying simulations, with large constant GM diffusivities in particular leading to a substantial overestimate. The overestimate of the abyssal cell appears to arise because the isopycnals are not steep enough above the Antarctic slope, compared to the 0.1° simulation (not shown). Consequently, the deep isopycnals are steeper away from Antarctica (as the mean slope of the isopycnals is strongly constrained by the surface and sponge boundary conditions), resulting in a stronger eddy-driven circulation throughout the channel. We will focus on the upper cell in the rest of the paper.

Together with the comparison of the ACC transport, we conclude that there is no optimal value for a constant GM diffusivity: large GM diffusivities reproduce the ACC transport well but misrepresent the MOC, and vice versa for small GM diffusivities. The variable GM diffusivities, and particularly the MEKE-based parameterization with topographic β effect (TMEKE), are able to reproduce both the ACC transport and the MOC reasonably well, although the lower cell MOC strength remains overestimated.

3) Bulk isopycnal interface height error ϵ

As a third metric for evaluation, we consider the bulk isopycnal interface height error, defined as

$$\epsilon \equiv \sum_{k=2}^{30} g_k' \left\langle \left(\overline{\eta}_{k,1^{\circ}} - \overline{\eta}_{k,0.1^{\circ}} \right)^2 \right\rangle, \tag{7}$$

where k is the isopycnal interface index, $g_k' = g(\sigma_k - \sigma_{k-1})/\rho_0$ is reduced gravity (g is the gravitational acceleration), $\eta_{k,1^\circ}$ and $\eta_{k,0,1^\circ}$ is the kth isopycnal interface height from the 1° and 0.1° simulations, respectively, $\overline{(\cdot)}$ denotes a temporal mean, and $\langle \cdot \rangle$ denotes a horizontal average over the whole domain (cf. Jansen et al. 2019). The interface height error ϵ measures the non-eddying models' ability to reproduce the temporally averaged density structure of the eddy-resolving simulation, with small ϵ indicating an accurate representation.

We find that the simulations using the TMEKE parameterization have the smallest isopycnal interface height error ϵ in both cases—with and without the sponge layer, as shown in Fig. 5. Comparing the two panels in Fig. 5 we find again that there is no optimal value for the constant GM diffusivity, $\kappa_{\rm GM}$: while an intermediate GM diffusivity leads to a smaller error in the simulations without the sponge layer, it actually results in a larger error in the simulations with the sponge layer. We also notice that the overall amplitude of the isopycnal interface height error is smaller in the simulations with a sponge layer, as the density structure is more tightly constraint by the boundary conditions.

In the rest of this paper, we will focus on four formulations of the GM diffusivity that provide reasonably good results in the reference configuration: two values of constant κ_{GM} (κ_4 and κ_7), the Visbeck scheme, and the TMEKE parameterization.

²Replacing total zonal velocity by geostrophic zonal velocity leads to qualitatively similar results and does not change our conclusions in this work.

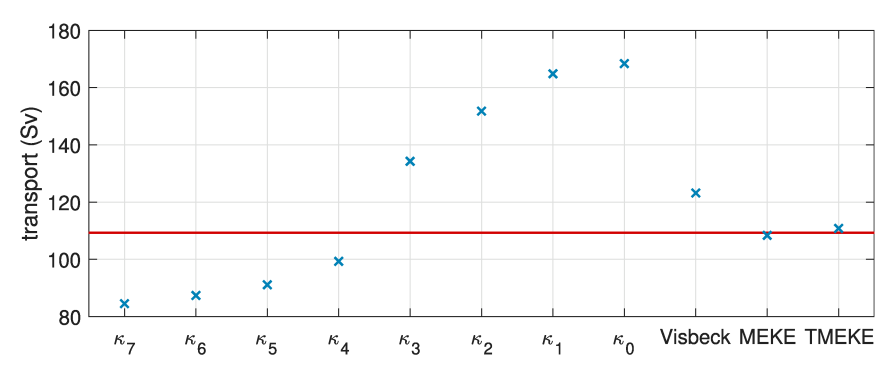


FIG. 3. Baroclinic ACC transport using different eddy parameterizations in the reference experiments (full topography, $\tau_0 = 0.2 \, \text{Pa}$) without northern sponge layer. The horizontal line denotes the ACC transport in the 0.1° simulation; blue crosses indicate the transport in the 1° simulations using the various eddy parameterizations denoted on the x axis (cf. Table 2).

b. The sensitivity of ACC transport to wind stress changes

In this section we focus on the response of the baroclinic ACC transport to changes in surface wind stress. To allow for an easier comparison to the established theories, we start with results from the flat-bottom channel simulations, before proceeding to the full topography setup. We will show that the ACC transport sensitivity is significantly overestimated by the coarse-resolution simulations in the flat-bottom setup, because the parameterizations underestimate the sensitivity of the transient eddy diffusivity. By contrast, in the presence of topography, the sensitivity of the ACC transport is only slightly overestimated by the coarse-resolution simulations, as stationary eddies play a dominant role.

1) ACC TRANSPORT RESPONSE IN THE FLAT-BOTTOM CHANNEL

In the flat-bottom simulations, all eddy parameterizations lead to a significant overestimate of the ACC transport response to wind stress changes, especially when a constant κ_{GM} is employed (Fig. 6). This result is expected for constant or insufficiently sensitive κ_{GM} because eddy fluxes will be increasingly inefficient at flattening the isopycnals as wind stress increases, resulting in a larger baroclinic ACC transport than in the eddyresolving simulation (cf. Munday et al. 2013; Mak et al. 2018). To test the hypothesis that the overestimate of the ACC transport sensitivity results from an underestimate of the sensitivity of the eddy diffusivity, we compare the prescribed or predicted GM diffusivities to the resolved meridional eddy buoyancy diffusivity in the high-resolution simulations (cf. Viebahn and Eden 2010). The domain averaged meridional transient eddy buoyancy diffusivity κ_{tr}^{ν} , from the 0.1° simulations is estimated as

$$\kappa_{\rm tr}^{y} = -\frac{\left\{ \left[\overline{v'b'} \right] \left[\partial_{y} \overline{b} \right] \right\}}{\left\{ \left[\partial_{y} \overline{b} \right]^{2} \right\}},\tag{8}$$

where $\{\cdot\}$ denotes a volumetric domain average, $(\cdot)'$ denotes a departure from the temporal average, v is the meridional velocity, and $b = -g(\rho - \rho_0)/\rho_0$ is the buoyancy.³ Correspondingly, κ_T^v in the 1° simulations with a variable GM diffusivity is computed as

$$\kappa_{\rm tr}^{y} = -\frac{\left\{ \left[-\overline{\kappa_{\rm GM}} \partial_{y} \overline{b} \right] \left[\partial_{y} \overline{b} \right] \right\}}{\left\{ \left[\partial_{y} \overline{b} \right]^{2} \right\}},\tag{9}$$

where $\kappa_{\rm GM}$ denotes the GM diffusivity, which is here assumed to represent the effect of transient eddies. (We confirmed that resolved transient eddies are negligible in the coarse-resolution simulations.) The motivation for the specific averaging in Eqs. (8) and (9) is documented in appendix B.

The sensitivity of κ_{tr}^{y} to wind stress changes qualitatively explains the discrepancy of the ACC response across simulations (cf. the left and right panels of Fig. 6). By definition, κ_{tr}^{y} remains constant in the κ_4 and κ_7 simulations, and these consequently have the most sensitive ACC transport response. Focusing on the three groups of simulations that either resolves eddies (0.1°) or have implemented a variable κ_{GM} (Visbeck and TMEKE), we further observe an inverse relationship between the sensitivities of κ_{tr}^{y} and ACC transport: the weakest ACC response among the three is obtained in the eddy-resolving simulation, which is associated with the most sensitive κ_{tr}^{y} response, while the strongest ACC response is obtained with the Visbeck scheme, which shows the lowest sensitivity in κ_{tr}^{y} . These observations support the hypothesis that an underestimate of the GM diffusivity sensitivity will lead to an overestimate of the sensitivity of the baroclinic ACC transport.

Another noteworthy result in Fig. 6 is that among all the five suites of simulations, the trend of the baroclinic ACC transport always saturates as wind stress increases, i.e., the response of the ACC transport to wind stress is sublinear [which is also seen in the constant κ_{GM} simulations of Mak et al. (2018, their Fig. 1)]. This sublinear tendency is not

³ Notice that although our numerical simulations employ isopycnal coordinates, Eq. (8) is defined using *z*-coordinate diagnostics, which are provided by MOM6 via run-time coordinate mapping. A *z*-coordinate formulation has been favored to avoid ambiguities in the definition of eddy fluxes and GM transport in the presence of isopycnal outcrops and nonzero vertically integrated eddy volume flux (Khani et al. 2019).

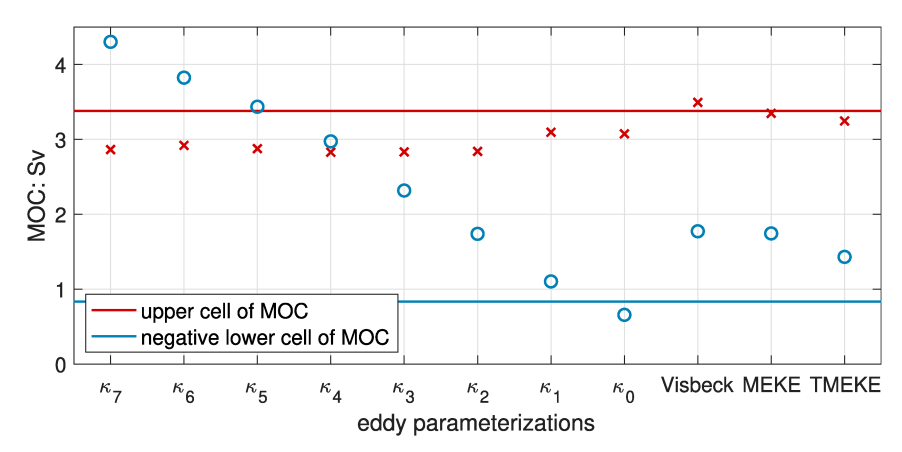


FIG. 4. Upper and lower cell MOC magnitude with different eddy parameterizations in the reference case with sponge layer (full topography, $\tau_0=0.2\,\mathrm{Pa}$). Horizontal lines denote results from the 0.1° reference simulation. Maroon crosses (blue open circles) denote the upper (lower) cell MOC from the 1° simulations. Notice that we are plotting the absolute values of the lower cell strength, whose streamfunction is by definition negative.

consistent with simple scaling arguments, which suggest that in the adiabatic limit:

$$T_{\rm ACC} \sim -\frac{\Delta b L_y^2 \tau^2}{\rho_0^2 f^3 \kappa_{\rm tr}^{y^2}},\tag{10}$$

where Δb is the meridional buoyancy contrast across the channel, L_y is the latitudinal width of the channel, τ is the domain averaged surface wind stress, and f is a characteristic value for the Coriolis parameter in the ACC [see appendix D for the derivation of Eq. (10)]. For constant $\kappa_{\rm GM}$ and hence constant $\kappa_{\rm tr}^{\nu}$ (i.e., the κ_7 and κ_4 cases), the ACC transport is thus expected to increase with the square of the wind stress, which is clearly inconsistent with the results of Fig. 6.

We argue that, at least in the constant κ_{GM} cases, the saturating trend of the baroclinic ACC transport at high winds is not due to the intensified mesoscale eddies but arises from a simple geometric constraint on the baroclinic transport. Specifically, the scaling argument in Eq. (10) starts to break down once isopycnals in the ACC start intersecting with the bottom of the ocean, at which point the sensitivity of the baroclinic transport to further wind stress increase starts to decline. Eventually, the transport will approach a theoretical limit, which is achieved when all isopycnals become vertical and the meridional buoyancy gradient becomes equal to the prescribed surface gradient throughout the depth of the ocean. A toy model that captures the effect of isopycnals intersecting with the sea floor is discussed in appendix E, and yields qualitatively similar results as seen in Fig. 6.

ACC TRANSPORT RESPONSE WITH FULL TOPOGRAPHY

In the presence of topography, the simulations with parameterized eddies (especially with variable κ_{GM}) only slightly overestimate the sensitivity of the ACC transport to wind stress changes, when compared to the eddy-resolving simulations (Fig. 7a). Moreover, the overestimate is not always due to an

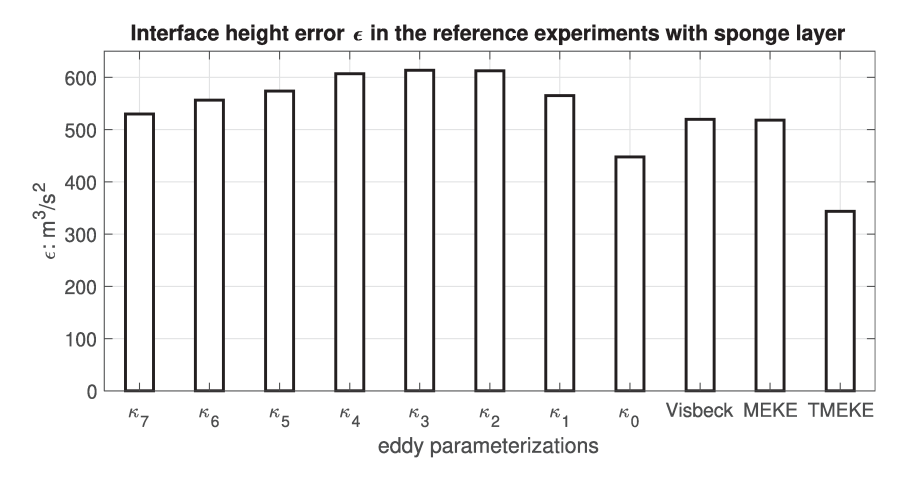
underestimate of the parameterized transient eddy diffusivity $\kappa_{\rm tr}^{\rm y}$. Comparing Figs. 7a and 7b, we find, for example, that $\kappa_{\rm tr}^{\rm y}$ is slightly more sensitive to wind stress changes with TMEKE than in the high-resolution simulations, yet the ACC transport is also more sensitive in the simulations using TMEKE.

The key to understanding the sensitivity of ACC transport to wind stress changes in the simulations with topography is the role of standing eddies. To capture this influence we compute a mean stationary eddy buoyancy diffusivity, analogously to the transient eddy diffusivity as

$$\kappa_{\rm st}^{y} = -\frac{\left\{ \left[\overline{v}^{*} \overline{b}^{*} \right] \left[\partial_{y} \overline{b} \right] \right\}}{\left\{ \left[\partial_{y} \overline{b} \right]^{2} \right\}},\tag{11}$$

where an asterisk denotes a departure from the zonal mean.

The magnitude and sensitivity of the stationary diffusivity is much higher than that of the transient diffusivity (Fig. 7b vs Fig. 7c), supporting the conclusion that, in the presence of topography, it is insufficient to consider only transient eddies to understand the ACC transport response to wind stress changes. Moreover, the sensitivity of κ_{st}^{y} to wind stress changes appears to compensate to some degree for the diverging sensitivities in the parameterized κ_{tr}^{y} , such that the combined eddy diffusivities are relatively similar across simulations configured with different eddy parameterizations and resolutions. The adequate representation of the combined diffusivity in the coarseresolution simulations explains their ability to capture the ACC transport sensitivity reasonably well. The simulations with the relatively large constant GM coefficient, κ_7 , remain as somewhat of an outlier, as their ACC transport falls outside of the spread of the other simulations, even though the combined diffusivity falls within the range of the others, at least at strong wind stress. Nevertheless, we conclude that it is crucial to take into account the full set of "eddies," including both transient and stationary components, to understand the sensitivity of the ACC transport. Our results moreover



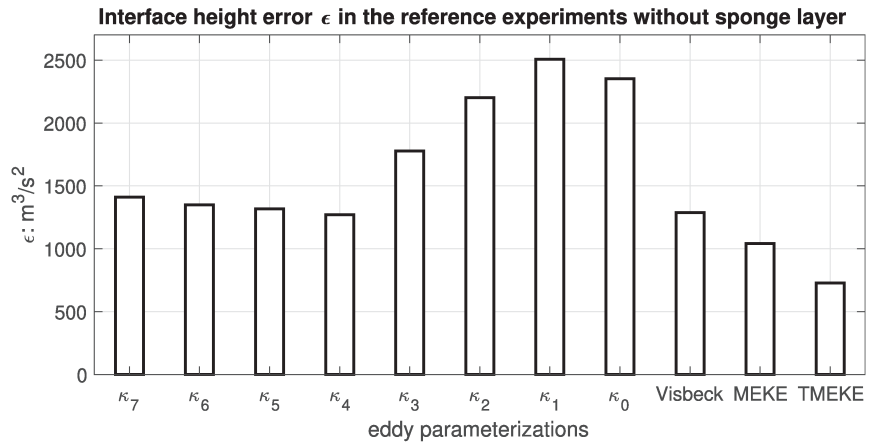


FIG. 5. Isopycnal interface height error ϵ , as defined in Eq. (7), in the reference case: $\tau_0 = 0.2 \, \text{Pa}$, with full topography, (top) with and (bottom) without the sponge layer (notice the different y axes in the two panels).

suggest that even simulations with constant κ_{GM} are potentially able to reasonably represent the ACC transport under varying wind stress, as long as topographic features and the associated standing eddies can be resolved adequately.

An alternative approach to account for standing meanders, that has been taken in some previous studies, is to apply a zonal average along streamlines or time-mean buoyancy contours (e.g., Karsten and Marshall 2002; Abernathey and Cessi 2014;

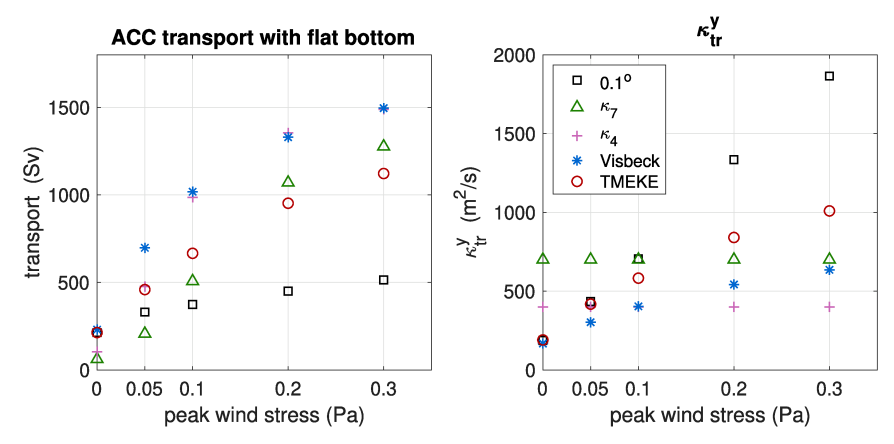


FIG. 6. The response of (left) baroclinic ACC transport and (right) meridional transient/GM diffusivity to surface wind stress changes in the flat-bottom setup without sponge layer.

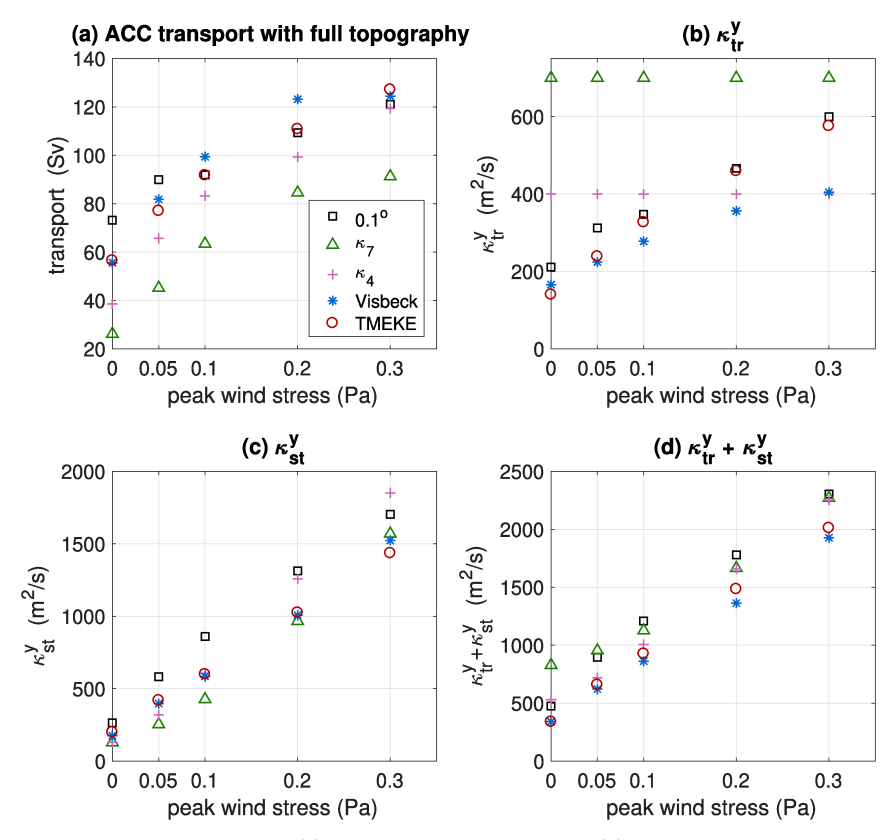


FIG. 7. The response of (a) baroclinic ACC transport, (b) transient/GM diffusivity, (c) stationary eddy buoyancy diffusivity, and (d) combined total eddy buoyancy diffusivity to changes in surface wind stress in the simulations with full topography and no sponge layer.

Thompson and Naveira Garabato 2014). In this framework, the standing meanders, by construction, do not appear explicitly, but they enhance cross-contour transport through the stretching of buoyancy contours and associated sharpening of the local gradients (cf. Nakamura 1996, 2001; Abernathey and Cessi 2014). Based on this idea, we derive an effective diffusivity diagnostic in appendix C that directly illustrates the effect of standing meanders via contour stretching. The stretching effect not only increases with wind stress, but also partially compensates for differences in the transient eddy diffusivity. Such compensation may be expected as a large transient eddy buoyancy diffusivity will inhibit the formation of sharp meanders and vice versa.

c. The sensitivity of the MOC to wind stress changes

In this section we focus on the response of the MOC to changes in surface wind stress. We will first analyze how topography affects the MOC response to wind stress changes in the eddy-resolving simulations, before considering the representation of MOC changes with parameterized eddies. We show that in the flat-bottom setup, eddy compensation is relatively weak and the MOC response is almost perfectly reproduced by coarse-resolution simulations with eddy parameterizations, but this result arises from a peculiar compensation between errors in the responses of the eddy diffusivity and isopycnal slope. Adding topography significantly suppresses the MOC response

to wind stress changes, just as found for the ACC transport, and the sensitivities of MOC, isopycnal slopes, and eddy diffusivity are all reasonably well represented by our coarse-resolution simulations.

1) MOC RESPONSE IN EDDY-RESOLVING SIMULATIONS

Topography again significantly suppresses the response of the MOC to surface wind changes, leading to a much smaller sensitivity than in the flat-bottom channel (Fig. 8). Compared to the theoretical maximum Ekman transport, some eddy compensation (i.e., a reduced residual MOC response compared to the Ekman-driven MOC) is observed even in the absence of topography, but the degree of compensation becomes significantly more pronounced in the presence of topography. Therefore, topography appears to significantly reduce the response of the MOC to changes in surface wind stress, through the effect of stationary eddies.

This dominant role of stationary eddies is confirmed by decomposing the residual MOC streamfunction into zonal and temporal mean flow (hereafter: mean flow), stationary eddy, and transient eddy components (Fig. 9). The residual MOC, mapped into depth space, is computed as

$$\psi(y,z) \equiv \psi(y,\sigma(y,z)) = \oint_{x} \int_{\sigma_{s}}^{\sigma(y,z)} \overline{v(x,y,\hat{\sigma}) \cdot h(x,y,\hat{\sigma})} \, d\hat{\sigma} \, dx.$$
(12)

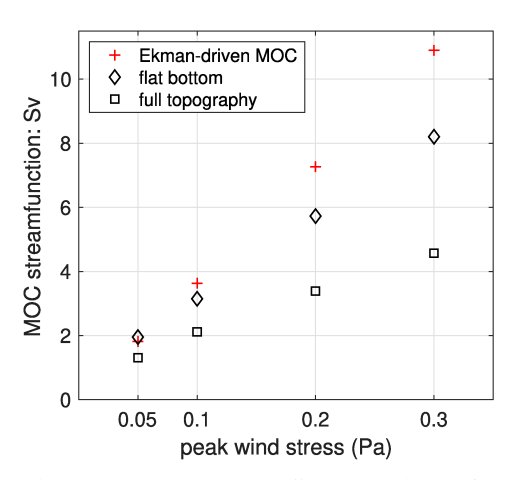


FIG. 8. The response of the upper cell MOC to changes in surface wind stress in the 0.1° simulations with sponge layer.

where $\sigma(y,z)$ is the isopycnal with mean depth z, i.e., the inverse of $\overline{z}(y,\sigma)$ (e.g., Young 2012) and σ_s is the minimum potential density at the surface.

We then decompose Eq. (12) into a temporal mean and a transient component. The temporal mean component is

$$\overline{\psi}(y,z) \equiv \oint_{x} \int_{\sigma_{s}}^{\sigma(y,z)} \overline{v}(x,y,\hat{\sigma}) \cdot \overline{h}(x,y,\hat{\sigma}) \, d\hat{\sigma} \, dx, \tag{13}$$

and the transient component is

$$\psi_{tr}(y,z) \equiv \psi - \overline{\psi} = \oint_{x} \int_{\sigma_{\epsilon}}^{\sigma(y,z)} \frac{v'(x,y,\hat{\sigma}) \cdot h'(x,y,\hat{\sigma})}{v'(x,y,\hat{\sigma}) \cdot h'(x,y,\hat{\sigma})} d\hat{\sigma} dx. \quad (14)$$

The temporal mean MOC $\overline{\psi}$ is further decomposed into an Eulerian zonal mean and a stationary eddy component. The Eulerian zonal mean part is defined based on an average at fixed depth, such that

$$[\overline{\psi}](y,z) \equiv \oint_{y} \int_{z_{s}}^{z} \overline{v}(x,y,\hat{z}) \, d\hat{z} \, dx, \qquad (15)$$

where z_s is sea surface height.⁴

Last, the stationary eddy component ψ_{st} is

$$\psi_{\rm et}(y,z) \equiv \overline{\psi} - \left[\overline{\psi}\right]. \tag{16}$$

The dominant role of stationary eddies in counterbalancing the response of the wind-driven mean flow component to wind stress changes is clearly demonstrated in Fig. 9. While the transient eddies also intensify with wind stress, thus contributing to eddy compensation, their role is significantly smaller than that of the stationary eddies.

2) MOC RESPONSE WITH PARAMETERIZED EDDIES IN THE FLAT-BOTTOM CHANNEL

In the flat-bottom channel, we find, somewhat surprisingly, that the coarse-resolution simulations with all eddy parameterizations almost perfectly reproduce the response of the MOC to wind stress changes (Fig. 10a). However, it turns out that this perfect representation is caused by a compensating effect between the responses of the transient eddy diffusivity and isopycnal slopes, neither of which is correctly represented in the coarse-resolution simulations, but together they provide the correct response of the residual MOC.

This compensating effect can be illustrated via the residual MOC framework proposed by Marshall and Radko (2003), where the MOC is approximated as the sum of the wind-driven and transient eddy-induced components:

$$\psi \approx \left[\overline{\psi}\right] + \psi_{\rm tr} \approx -\frac{\tau}{\rho_0 f} + \kappa_{\rm tr}^{y} s$$
 (17)

where $s = -\partial_y \overline{b}/\partial_z \overline{b}$ is the isopycnal slope. The response of ψ to (small) wind stress changes can then be approximated as [cf. Abernathey et al. (2011)]

$$\partial_{\tau}\psi \approx -\frac{1}{\rho_0 f} + \partial_{\tau}\kappa_{\rm tr}^{y} s + \kappa_{\rm tr}^{y} \partial_{\tau} s.$$
 (18)

As is shown in Fig. 11a, the sensitivity of κ_{tr}^{y} to wind stress changes is underestimated in all parameterized simulations. Instead, the response of the isopycnal slopes is overestimated by the parameterized simulations (Figs. 11b-f). The simulations with constant GM diffusivity (κ_4 and κ_7) show the largest response in isopycnal slopes-developing a pronounced "V" shape in the isopycnal structure at strong winds. In the 0.1° simulation, where the eddy diffusivity is most sensitive to wind stress changes, the isopycnal slopes instead change relatively little, except in the abyssal ocean and at the highest latitudes. The simulations using Visbeck or TMEKE parameterizations show intermediate sensitivities in both κ_{tr}^{y} and isopycnal slopes. Why this almost perfect compensation between the sensitivities of κ_{tr}^y and isopycnal slopes exists, unfortunately, remains not clear to us, although the strong constraint imposed by the sponge layer appears likely to affect this result.

The compensating effect illustrated in Fig. 11 is reminiscent of the results shown in Viebahn and Eden (2010, their Fig. 5), whose eddy-permitting simulations produce the same amplitude of residual MOC response at different resolutions, due to a similar compensating effect. However, different from our result, Viebahn and Eden (2010) do not find the same compensation effect in their non-eddying simulations with parameterized eddies. Whatever the specific reason for the almost perfect error compensation in our simulations is, it is

⁴ One could alternatively also define the time and zonal mean component based on isopycnal averages, as done, e.g., in Bishop et al. (2016). However, using isopycnal averaging will lead to a systematic eddy Ekman transport component (directed opposite to the net Ekman transport), because the Ekman transport is distributed over at least one isopycnal layer such that the Ekman velocity in that layer is inversely correlated with the layer thickness. We therefore here choose to isolate the Eulerian mean component as it better captures the wind-driven Ekman transport contribution. However, our main results are not sensitive to this choice.

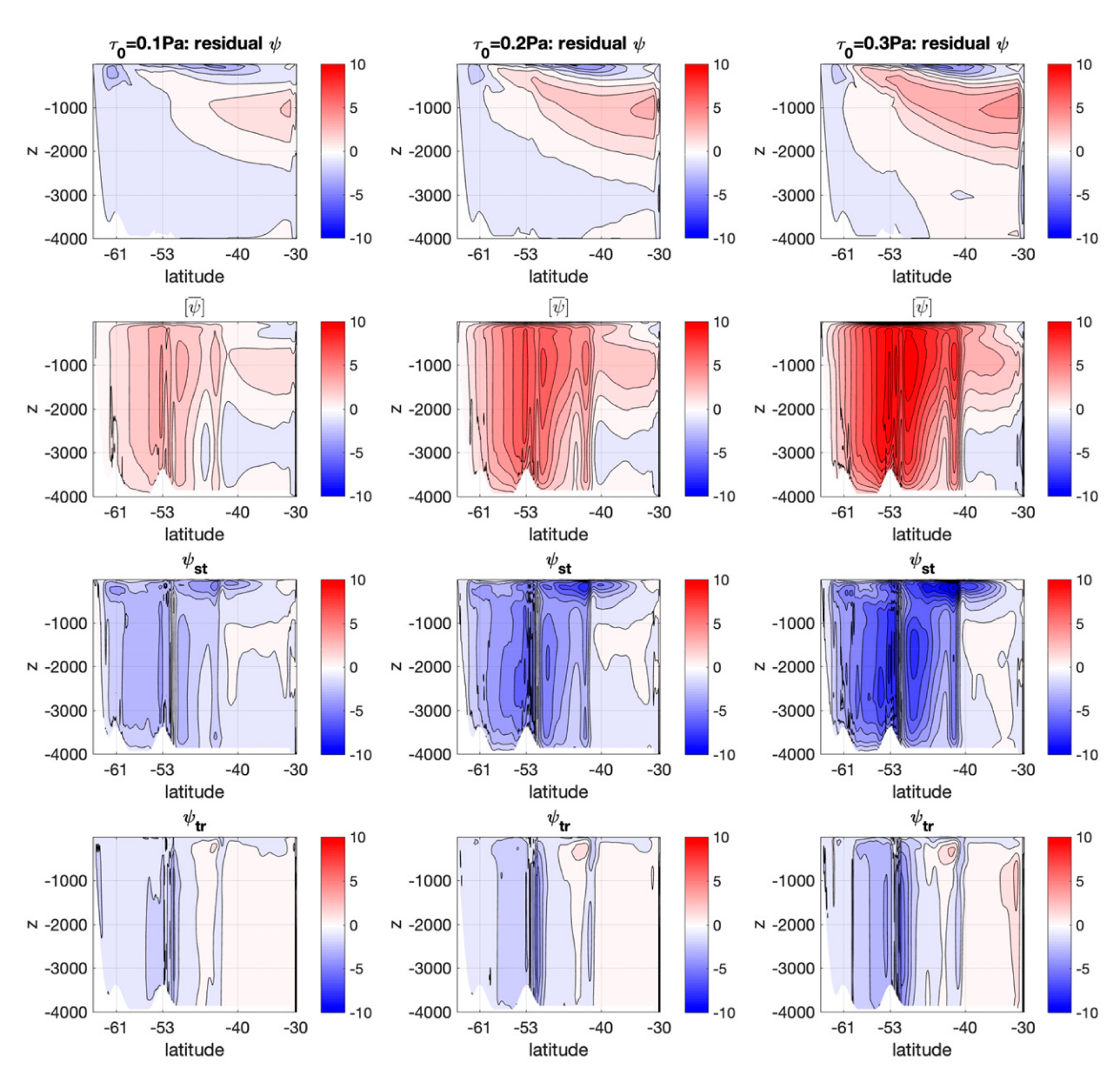


FIG. 9. The response of MOC components to changes in surface wind stress in 0.1° simulations with full topography and northern sponge layer. Each column shows the MOC components for one value of wind stress (left: $\tau_0 = 0.1$ Pa; center: $\tau_0 = 0.2$ Pa; right: $\tau_0 = 0.3$ Pa). The rows from top to bottom correspond to residual MOC ψ , zonal and temporal mean flow $[\overline{\psi}]$, stationary eddies $\psi_{\rm st}$, and transient eddies $\psi_{\rm tr}$. The contour interval is 1 Sv.

clear that the simulations with parameterized eddies do not adequately capture the response of the flat-bottom channel to wind stress changes.

3) MOC RESPONSE WITH TOPOGRAPHY

When topography is included, the MOC response is reasonably well represented by the coarse-resolution simulations (Fig. 10b), and, unlike in the flat-bottom simulations, the adequate MOC response does not arise from compensating errors. Instead, the sensitivities of both the total eddy diffusivity (i.e., $\kappa_t^{\nu} + \kappa_{st}^{\nu}$) and isopycnal slope are relatively well captured in all coarse-resolution simulations, as is illustrated in Fig. 12.

The sensitivity of the total eddy diffusivity to changes in the wind stress is again strongly modulated by the effect of standing meanders (not shown) which reduces the sensitivity to the representation of transient eddies. The isopycnal structure is comparatively insensitive to wind stress changes in all simulations, indicating that any compensation is dominantly caused by the increase in the total eddy diffusivity with wind stress.

5. Discussion

In this study we employ four versions of an idealized channel model to study the response of Southern Ocean circulation to

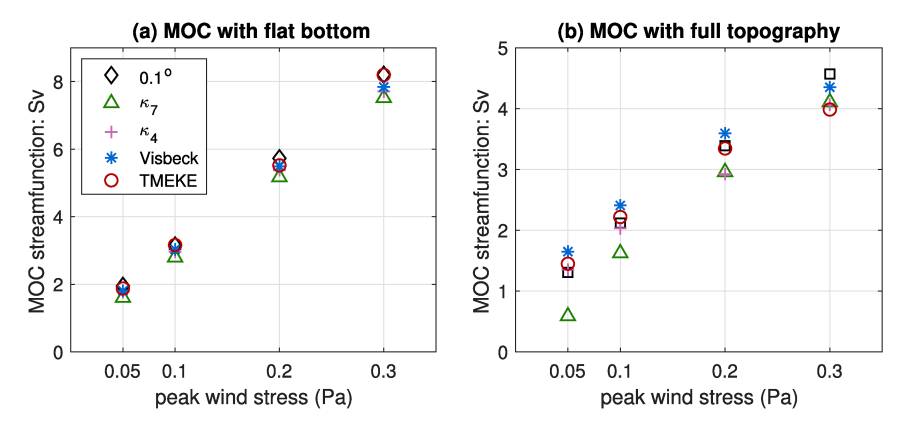


FIG. 10. The response of the upper cell MOC to changes in surface wind stress in the 0.1° and 1° simulations with sponge layer, using (a) the flat-bottom setup and (b) the full topography setup.

changes in surface wind stress. The idealized setup allows us to perform a large suite of equilibrated simulations under varying wind stresses and resolutions, but naturally also comes with a number of limitations.

Perhaps the most significant limitation of our study is the need for a northern boundary condition. To investigate the response of the ACC transport to wind stress changes we use an adiabatic northern boundary condition, which allows isopycnals to adjust freely at the northern boundary. By construction, this boundary condition only allows a very weak residual MOC, balanced by diffusion within the Southern

Ocean, and hence amounts to assuming almost perfect eddy compensation: any increase in the wind-driven MOC needs to be almost completely compensated by the response in the eddy-induced MOC. However, when a basin is included to the north of the channel, previous studies (e.g., Gnanadesikan 1999; Nikurashin and Vallis 2012) suggest that any changes in the depth of the isopycnals in the basin should lead to a response in the rate of northern deep water formation and hence a change in the residual MOC in the Southern Ocean, which would exclude the possibility of perfect eddy compensation without perfect eddy saturation.

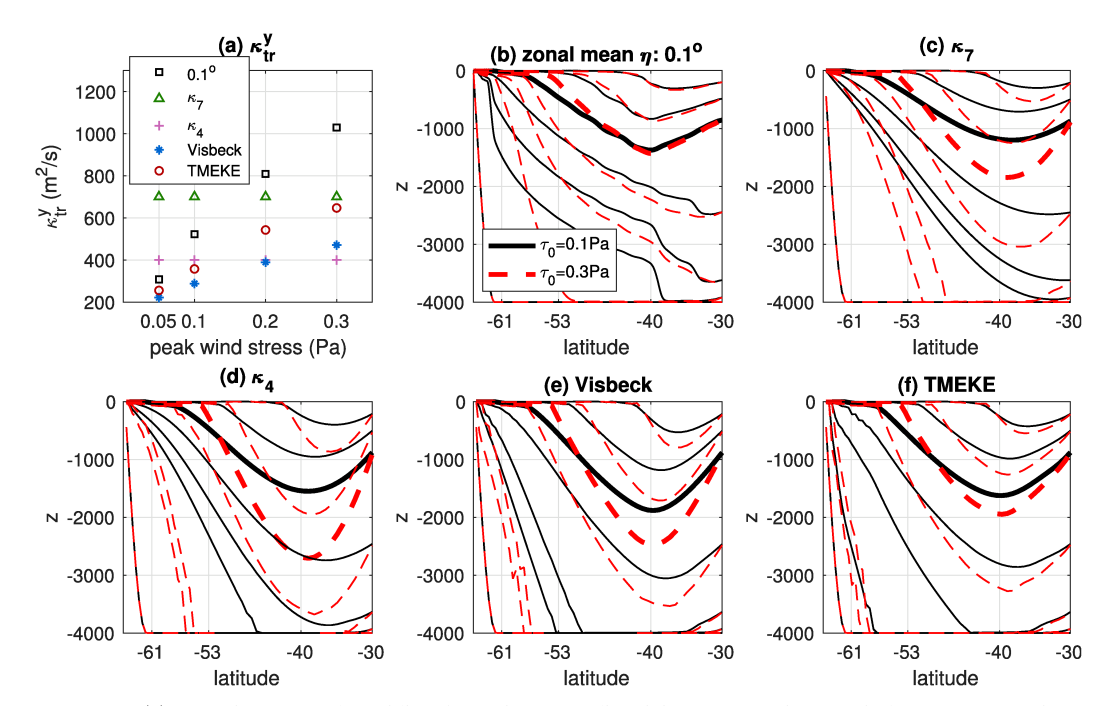


FIG. 11. (a) Domain averaged meridional transient GM diffusivity as a function of wind stress from various simulations in the flat-bottom setup with sponge layer at the northern boundary. (b)–(f) Zonal mean isopycnal structure under wind stress $\tau_0 = 0.1$ Pa (black solid lines) and $\tau_0 = 0.3$ Pa (red dashed lines). Bold lines denote the $\sigma = 1037$ kg m⁻³ isopycnal, along which the upper MOC cell strength in Fig. 10 is evaluated.

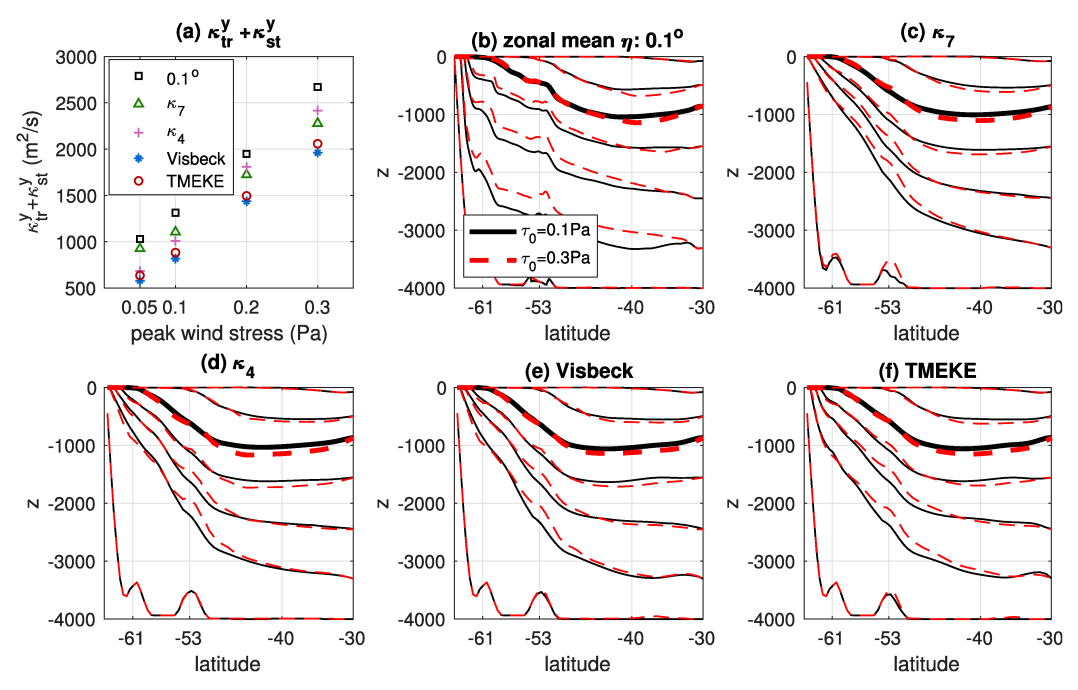


FIG. 12. As in Fig. 11, but for the simulations with topography. Also notice that (a) shows the combined stationary plus transient eddy buoyancy diffusivity, $\kappa_{\rm tr}^{\rm y} + \kappa_{\rm st}^{\rm y}$.

To study the MOC response to wind stress changes we adopt a sponge layer at the northern boundary, where the buoyancy is restored to a reference profile. The restoring crudely mimics water mass transformation processes that occur in the basins north of the Southern Ocean, and it is crucial to maintain a nontrivial residual MOC. However, the sponge layer essentially prohibits any substantial change of the stratification at the northern boundary, even as wind stress changes significantly. The circulation simulated with the sponge layer configuration may be a reasonable approximation for the short-time-scale response of the real ocean, before the stratification in the basins has time to adjust. By contrast, this model configuration is probably unable to address the question of how the real MOC responds to wind stress changes in its final, equilibrium state. An alternative approach is to implement an enhanced diapycnal mixing at the northern boundary, as adopted, e.g., by Hogg (2010). However, this approach will generally only induce a counterclockwise MOC that is more similar to the abyssal cell. To quantitatively gauge the role of stratification adjustments in the basin on different time scales, a direct comparison to interhemispheric model simulations is needed, which is part of ongoing work.

Our results may also depend on the specifics of the topography, which has previously been shown to affect the response of the ACC transport to surface wind stress changes (Nadeau et al. 2013). In the current study, our topography is smooth enough to be reasonably well resolved, even in our coarse-resolution simulations. As a result we may expect that standing meanders excited by the topography can also be resolved reasonably well. Yet in the real ocean, topography spans a wide spectrum of spatial scales, and hence the ability of coarse-resolution models to capture the effects of stationary eddies is

likely to be more significantly impaired. How this difference impacts the conclusions of the current work needs to be addressed in the future.

Our results for the sensitivity of the ACC transport to wind stress changes differ from those of Mak et al. (2018), who find almost perfect eddy saturation in their eddy-permitting simulations. The perfect saturation is also largely captured by their coarse-resolution simulations configured with the GEOMETRIC eddy parameterization, but is not reproduced with a constant GM diffusivity. What explains the difference between our and their simulations remains unclear to us, although differences in the model geometry and the use of linear versus quadratic drag may be important.

Our results for the ACC transport sensitivity with topography are broadly consistent with those of Farneti et al. (2015). However, our results for the MOC response with topography seem to stand in contrast with those of Farneti et al. (2015) and Poulsen et al. (2018). Particularly, Farneti et al. (2015) find that GCMs that either are eddy-permitting or have implemented a κ_{GM} with 3D spatial structure tend to have a significantly higher degree of eddy compensation than the models whose κ_{GM} is constant or employs a 2D spatial structure. Yet our Fig. 10 shows that both a constant κ_{GM} (the κ_4 case) and a 2D varying κ_{GM} (Visbeck, TMEKE) are able to reproduce a similar degree of eddy compensation as the eddy-resolving simulations, due to the effect of stationary eddies, which allow a realistic representation of the total (stationary plus transient) eddy diffusivity (Fig. 12). One obvious difference in our study is the idealized model configuration, in particular the use of a sponge layer to restore the stratification at the northern boundary, as well as the relatively smooth simplified topography (as discussed

above). Perhaps even more importantly, the simulations in Poulsen et al. (2018) are only integrated for 17 years, and the GCMs in Farneti et al. (2015) are forced with wind stress changes over a 60-yr period, which leads to a strongly diabatic nonequilibrium MOC response pattern. The MOC changes in our fully equilibrated simulations instead are largely adiabatic in the interior, which adds a significant constraint on the MOC response. The time-dependent response of the ACC and MOC to wind stress changes will be addressed in a follow-up study.

6. Conclusions

The surface wind stress over the Southern Ocean has been increasing significantly for decades, yet the response of the Southern Ocean circulation to the wind stress change has not been fully understood. In this work we have used four versions of idealized models of the Southern Ocean to investigate the circulation response to changes in surface wind stress. We have explored the role of topography in modulating this response and tested several state-of-the-art eddy parameterizations to analyze in how far coarse-resolution simulations with parameterized eddies can reproduce the response, with and without topography. Our main finding is that some degree of both eddy saturation and compensation exist in our model, even in the absence of topography. However, topography significantly increases the degree of eddy saturation and compensation, by inducing strong stationary eddies that substantially amplify the effect of the transient eddies. The coarse-resolution simulations with parameterized eddies are able to reproduce the circulation response reasonably well in the presence of topography. Although state-of-the art eddy parameterizations with variable GM diffusivity generally perform better, the ACC and MOC responses to wind stress changes are surprisingly well captured even when using a constant GM diffusivity. We attribute this result to the key role played by standing meanders, which dominate the meridional buoyancy flux. In the absence of topography, however, the simulations with parameterized eddies struggle to represent an accurate ACC transport response. The MOC response is reproduced correctly, but only due to compensating errors in the responses of the eddy diffusivity and isopycnal slopes.

Our results highlight the importance of topography in modulating the response of the Southern Ocean circulation to changes in surface wind stress, which deserves more attention in future development and testing of eddy parameterizations. In the meantime, our results provide hope that GCMs with realistic topography are less sensitive to the choice of mesoscale eddy parameterizations than suggested by idealized flat-bottom models and theories.

Acknowledgments. We thank Dave Munday and an anonymous reviewer for their insightful comments, which helped to improve this manuscript. We also thank Robert Hallberg, Alistair Adcroft, and Zhihong Tan for their help with the configuration of our idealized models, and Noboru Nakamura and Tiffany Shaw for helpful conversations. Computational

resources for this project were generously provided by the University of Chicago Research Computing Center. We acknowledge support from the National Science Foundation (NSF) through Awards OCE-1536450 and OCE-1846821.

Data availability statement. The MOM6 version used for this paper is available on GitHub (DOI: 10.5281/zenodo.3905507). Parameter files for the specific simulations are also available on GitHub (DOI: 10.5281/zenodo.3903644).

APPENDIX A

Eddy Parameterizations

a. Visbeck scheme

The Visbeck scheme used in our model is based on Visbeck et al. (1997). It is implemented in MOM6 as

$$\kappa_{\rm GM} = \alpha l^2 \langle SN \rangle,$$
(A1)

where $\alpha=0.015$ is an empirical nondimensional coefficient, chosen as in Visbeck et al. (1997); $l=100\,\mathrm{km}$ in our setup, which allows us to roughly match the ACC transport and the upper cell MOC of the 0.1° simulations in the reference case; S is the isopycnal slope, N is the Brunt–Väisälä frequency, and $\langle \cdot \rangle$ denotes a vertical average.

b. MEKE

The MEKE scheme is based on Jansen et al. [2015, their Eq. (1)], and uses a prognostic equation for the vertically integrated subgrid mesoscale eddy kinetic energy:

$$\partial_t E = \dot{E}_{\rm GM} - \dot{E}_{\rm fric} - \nabla \cdot T,$$
 (A2)

where E is MEKE, $\dot{E}_{\rm GM}$ is the large-scale energy loss associated with the GM parameterization, $\dot{E}_{\rm fric}$ is the frictional dissipation of MEKE, and T is the horizontal transport of MEKE, here parameterized via a diffusion of MEKE with a diffusivity $\kappa_{\rm MEKE} = 1000\,{\rm m\,s^{-2}}$.

The mesoscale kinetic energy E is then combined with the mixing length l_M to form the GM diffusivity

$$\kappa_{\rm GM} = l_M \sqrt{\gamma_t^2 U_e^2},\tag{A3}$$

where $U_e = \sqrt{2E}$, $I_M = \alpha/(L_e^{-1} + L_A^{-1} + L_\Delta^{-1})$ ($\alpha = 0.12$ has been optimized based on the reference case; $L_e = U_e/(|S|N)$ is the Eady scale, $L_R = \sqrt{U_e/B}$ is the Rhines scale, and L_Δ is the grid spacing), and $\gamma_t^2 = \max[(1+50L_d/L_f)^{-1/4}, \ 1\times 10^{-4}]$ is an estimate for the ratio of barotropic to total EKE (with L_d the Rossby radius of deformation, $L_f = H/C_D$ the frictional halting scale, H the ocean depth, and $C_D = 0.003$ the quadratic drag coefficient). Additional details are provided in Jansen et al. (2015).

c. Topographic MEKE

The topographic MEKE formulation is similar to MEKE but considers the suppression of the GM diffusivity by the topographic β effect. Specifically, the Rhines scale L_R is

computed using a topographically modified barotropic potential vorticity gradient:

$$\beta^* = \sqrt{\left(\partial_x f - \frac{f}{H}\partial_x H\right)^2 + \left(\partial_y f - \frac{f}{H}\partial_y H\right)^2}.$$
 (A4)

APPENDIX B

Domain Averaged Meridional Transient and Stationary GM Diffusivity

The effective domain-averaged GM diffusivity in Eq. (8) is computed by minimizing the RMS error of the implied meridional eddy buoyancy flux. We aim to approximate the zonally averaged meridional transient eddy buoyancy flux $[\overline{v'b'}]$ in the 0.1° simulations with a representative transient eddy diffusivity κ_{tr}^y as

$$\left[\overline{\upsilon'b'}\right] = -\kappa_{\rm tr}^{y} \left[\partial_{y} \overline{b}\right] + \delta, \tag{B1}$$

where δ is the residual. Our goal is to find the κ_{tr}^{y} that minimizes the domain-averaged δ^{2} :

$$\begin{split} \left\{ \delta^{2} \right\} &= \left\{ \left(\left[\overline{\upsilon' b'} \right] + \kappa_{\text{tr}}^{y} \left[\partial_{y} \overline{b} \right] \right)^{2} \right\} = \left\{ \left[\overline{\upsilon' b'} \right]^{2} \right\} \\ &+ 2\kappa_{\text{tr}}^{y} \left\{ \left[\overline{\upsilon' b'} \right] \left[\partial_{y} \overline{b} \right] \right\} + \kappa_{\text{tr}}^{y2} \left\{ \left[\partial_{y} \overline{b} \right]^{2} \right\}. \end{split} \tag{B2}$$

Let $\partial_{\kappa_{tr}^y} \{\delta^2\} = 0$ and we retrieve Eq. (8). Similarly, for the 1° simulations, Eq. (B1) is replaced by

$$-\left[\overline{\kappa_{\rm GM}\partial_{y}b}\right] = -\kappa_{\rm tr}^{y}\left[\partial_{y}\overline{b}\right] + \delta, \tag{B3}$$

and following the same procedure we retrieve Eq. (9).

The derivation of Eq. (11) is almost identical to Eq. (8), except we replace $[\overline{v'b'}]$ in Eq. (B1) by $[\overline{v}^*\overline{b}^*]$.

APPENDIX C

Interpreting the Effect of Standing Eddies via Stretching of Mean Contours

In Eqs. (8), (9), and (11), the total eddy buoyancy flux across any latitude circle is defined in terms of the sum of a transient and a stationary component

$$F_{y} = L_{x} \left[\overline{v} * \overline{b} * + \overline{v'b'} \right] = -L_{x} (\kappa_{\rm st}^{y} + \kappa_{\rm tr}^{y}) \left[\partial_{y} \overline{b} \right], \tag{C1}$$

where L_x is the zonal length of the domain at this latitude.

An alternative streamwise mean perspective has also been taken by previous studies, where the zonal average is taken along temporarily averaged streamlines or buoyancy contours (Karsten and Marshall 2002; Abernathey and Cessi 2014). In this case, the standing eddy flux vanishes by construction, and the transport across a mean buoyancy contour $\overline{b} = b_0$ is

$$F_{b_0} \equiv \int_{\overline{b} = b_0} \overline{\nu_n' b'} \ ds \equiv \int_{\overline{b} = b_0} \overline{\mathbf{u}' b'} \cdot \frac{\nabla_z \overline{b}}{|\nabla_z \overline{b}|} \ ds = -\int_{\overline{b} = b_0} K_{\mathrm{tr}} |\nabla_z \overline{b}| \ ds \,, \tag{C2}$$

where $v_n \equiv \mathbf{u} \cdot \nabla_z \overline{b}/|\nabla_z \overline{b}|$ is the normal velocity across the buoyancy contour, ∇_z denotes the horizontal gradient (at constant z) and we defined a local (cross-contour) transient eddy buoyancy diffusivity as

$$K_{\rm tr} \equiv -\frac{\overline{\mathbf{u}'b'} \cdot \nabla_z \overline{b}}{|\nabla_z \overline{b}|^2}.$$
 (C3)

Following Nakamura (1996), the cross-contour flux in Eq. (C2) can be expressed as

$$\begin{split} F_{b_0} &= -\int_{\overline{b} = b_0} K_{\rm tr} |\nabla_z \overline{b}| \, ds = -\frac{\partial \mathscr{M} \left(K_{\rm tr} |\nabla_z \overline{b}|^2 \right)}{\partial b_0} \\ &= -\left\langle K_{\rm tr} |\nabla_z \overline{b}|^2 \right\rangle \frac{\partial A}{\partial b_0}, \end{split} \tag{C4}$$

where

$$\mathcal{A}(\cdot) \equiv \iint_{\overline{h} \le h_{\delta}} (\cdot) \, dA \tag{C5}$$

denotes an integral over the area delimited by the mean buoyancy contour $\overline{b}=b_0$, $A=\mathcal{M}(1)$, and $\langle(\cdot)\rangle\equiv\partial_A\mathcal{M}(\cdot)$ defines an average along the mean buoyancy contour. With an effective latitude, $Y(b_0)$, defined such that $L_x\partial_{b_0}Y=\partial_{b_0}A$ (Nakamura and Zhu 2010), we get

$$F_{b_0} = -L_x K_{\text{eff}} \frac{\partial b_0}{\partial Y}, \tag{C6}$$

where

$$K_{\text{eff}} = \frac{\left\langle K_{\text{tr}} | \nabla_{z} \overline{b} |^{2} \right\rangle}{|\partial_{Y} b_{0}|^{2}}.$$
 (C7)

Equations (C6) and (C7) illustrate that standing meanders increase the effective meridional buoyancy diffusivity via a stretching of buoyancy contours, which sharpens the local gradients. This effect is analog to the amplification of mixing by eddy-induced contour stretching discussed by Nakamura (1996), except we are here considering only the stretching effect of standing meanders, with the transient eddy diffusivity replacing microscale diffusion.

Assuming that $F_y \approx F_{b_0}$ and $|\partial_\gamma b_0|^2 \approx [\partial_y \overline{b}]^2$, comparison of Eqs. (C1) and (C6) shows that $K_{\rm eff} \approx \kappa_{\rm st}^y + \kappa_{\rm tr}^y$. Assuming further that, on average, $\langle K_{\rm tr} | \nabla_z \overline{b}|^2 \rangle \approx [K_{\rm tr} | \nabla_z \overline{b}|^2]$, the effective diffusivity can be approximated as

$$K_{\text{eff}} \approx \frac{\left[K_{\text{tr}} | \nabla_z \overline{b}|^2\right]}{\left[\partial_y \overline{b}\right]^2}.$$
 (C8)

Following the same argument as in appendix B, we can define a domain-averaged (cross-contour) transient buoyancy diffusivity as

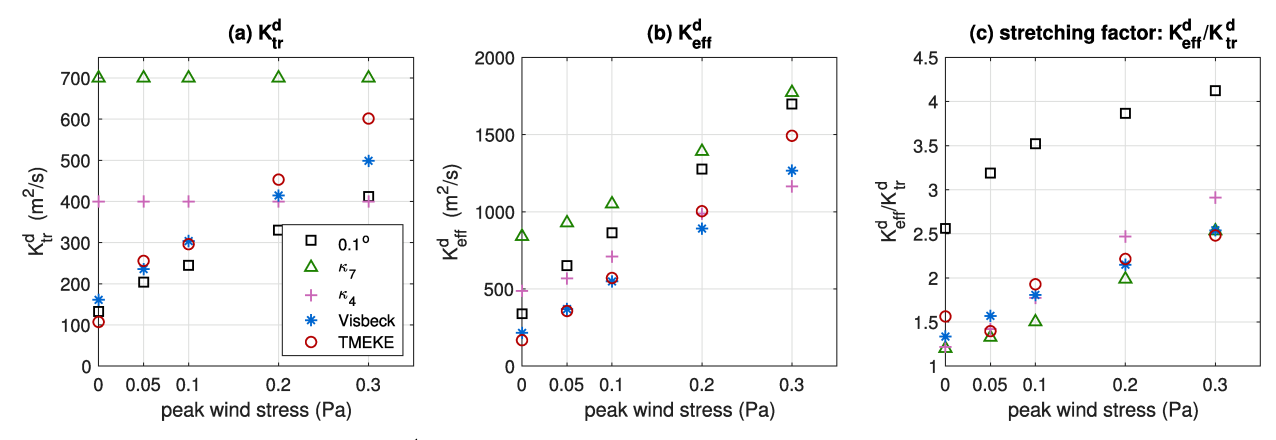


FIG. C1. (a) Transient GM diffusivity K_{tr}^d as a function of wind stress, in the simulations with full topography and no sponge layer. (b) Effective diffusivity K_{eff}^d as a function of wind stress in the same simulations. (c) The stretching factor, K_{eff}^d/K_{tr}^d .

$$K_{\text{tr}}^{d} = \frac{\left\{ K_{\text{tr}} | \nabla_{z} \overline{b} |^{2} \right\}}{\left\{ | \nabla_{z} \overline{b} |^{2} \right\}}, \tag{C9}$$

and a domain averaged effective diffusivity as

$$K_{\text{eff}}^{d} \equiv \frac{\left\{ K_{\text{tr}} | \nabla_{z} \overline{b}|^{2} \right\}}{\left\{ \left[\partial_{y} \overline{b} \right]^{2} \right\}} = K_{\text{tr}}^{d} \frac{\left\{ | \nabla_{z} \overline{b}|^{2} \right\}}{\left\{ \left[\partial_{y} \overline{b} \right]^{2} \right\}}. \tag{C10}$$

As shown in Fig. C1b, the effective diffusivity K_{eff}^d is qualitatively similar to the combined (stationary plus transient) diffusivity shown in Fig. 7d. As illustrated in Fig. C1c, the effective diffusivity K_{eff}^d is significantly amplified by the stretching effect, especially in the 0.1° simulations, where the stationary meanders are relatively strong, and the stretching effect increases with increasing wind stress. Moreover, for any given wind stress, the stretching effect tends to be stronger in simulations that have a small transient diffusivity and vice versa, therefore compensating to some degree (albeit not completely) for differences in the transient diffusivity. This compensating effect may be expected, as a large diffusivity tends to smooth standing meanders, and it is somewhat similar to the insensitivity of Nakamura's effective diffusivity to the magnitude of microscale diffusion (although true insensitivity cannot be expected, unless the stretching factor is much larger than one, which is not the case here).

APPENDIX D

A Simple Scaling for the Baroclinic ACC Transport in an Adiabatic, Flat-Bottom Channel

In an adiabatic limit, the residual circulation has to vanish and Eq. (17) reduces to

$$\kappa_{\rm tr}^{\rm y} s = \frac{\tau}{\rho_{\rm o} f},$$
(D1)

where $s \sim -h_0/L_y$, with h_0 the depth of the densest isopycnal at the northern boundary and L_y the width of the channel (Fig. D1a for a schematic), and τ is the wind stress. Therefore, h_0 scales as

$$h_0 \sim -\frac{\tau L_y}{\rho_0 f \kappa_{\text{tr}}^y}.$$
 (D2)

Assuming that the baroclinic ACC flow follows the thermal wind relation, we obtain a scaling for the baroclinic zonal velocity as

$$u \sim -\frac{h_0 \Delta b}{f L_{\nu}}.$$
(D3)

Integrating Eq. (D3) and using Eq. (D2) yields the scaling in Eq. (10):

$$T_{\rm ACC} \sim u h_0 L_y \sim -\frac{\Delta b L_y^2 \tau^2}{\rho_0^2 f^3 \kappa_{\rm tr}^{v2}}.$$
 (D4)

APPENDIX E

A Toy Model for the Baroclinic ACC Transport in a Channel with Finite Depth

To understand the effect of isopycnal incrops on the baroclinic ACC transport at strong wind stress, we construct a simple toy model, assuming 1) a zonally symmetric and flatbottomed channel, with a prescribed constant surface buoyancy gradient; 2) isopycnal slopes are constant with depth and latitude; 3) variations in the Coriolis parameter are negligible; and 4) the residual MOC, balanced by diapycnal mixing within the channel, can be approximated as $\psi \approx -\kappa_d / s$, where κ_d is the diapycnal diffusivity (Ito and Marshall 2008).

Under these assumptions, Eq. (17) can be written as

$$\kappa_d \frac{L_y}{h_0} = \frac{\tau}{\rho_0 f} + \kappa_{\text{tr}}^y \frac{h_0}{L_y},\tag{E1}$$

where $\kappa_d = 5 \times 10^{-5} \,\mathrm{m}^2 \,\mathrm{s}^{-1}$, $h_0 = -sL_y$ is the depth of the densest isopycnal at the northern boundary, $\rho_0 = 1037 \,\mathrm{kg} \,\mathrm{m}^{-3}$, and $f = -1 \times 10^{-4} \mathrm{s}^{-1}$. Solving Eq. (E1) for h_0 we find

$$h_0 = \left[\frac{-\tau}{2\rho_0 f \kappa_{\text{tr}}^y} + \sqrt{\left(\frac{-\tau}{2\rho_0 f \kappa_{\text{tr}}^y} \right)^2 + \frac{\kappa_d}{\kappa_{\text{tr}}^y}} \right] L_y. \tag{E2}$$

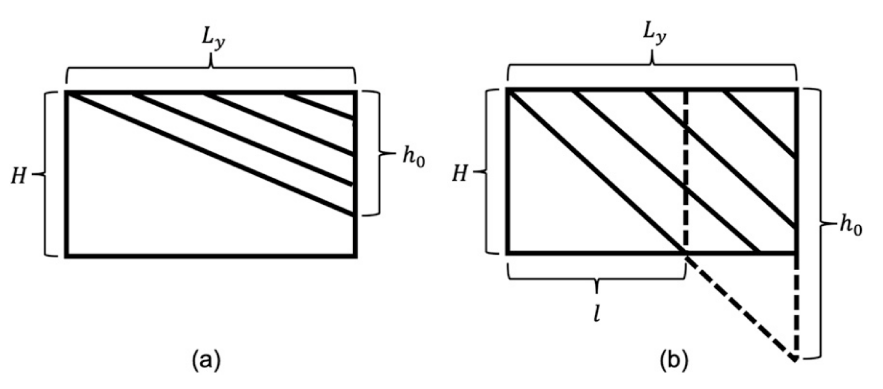


FIG. D1. Schematics for the ACC toy model. In each panel, south is on the left. Shown are two scenarios, where (a) $|s| \le H/L_v$: no incropping occurs and (b) $|s| > H/L_v$: incropping occurs.

Notice that once the densest isopycnal begins to incrop with the sea floor (Fig. D1b), h_0 becomes a hypothetical depth, which is the depth of this isopycnal at the northern boundary if the ocean were infinitely deep. In this case, we use l to denote the distance between the southern boundary and the incropping location of this densest isopycnal (with $l = L_y$ if no incropping occurs):

$$l = \min\left(\frac{H}{h_0}L_y, L_y\right). \tag{E3}$$

Meanwhile, the thermal wind relation, $\partial_z u_{bc} = -1/f \partial_y b$, provides the baroclinic zonal velocity as

$$u_{\rm bc}(y,z) = -\frac{1}{f} \int_{-h(y)}^{z} \partial_y b \, dz = -\frac{\Delta b}{fL_y} [h(y) + z],$$
 (E4)

where $h(y) = \min(h_0 y/L_y, H)$ is the depth of the densest isopycnal interface, below which the stratification and the baroclinic zonal flow both vanish. Using that $h(y) = h_0 y/L_y$ for y < l and h(y) = H for $y \ge l$, we can compute the baroclinic ACC transport as

$$\begin{split} T_{\text{ACC}} &= \int_{0}^{L_{y}} \int_{-h(y)}^{0} u_{\text{bc}}(y, z) \, dz \, dy \\ &= -\frac{\Delta b}{fL_{y}} \int_{0}^{L_{y}} \frac{h(y)^{2}}{2} \, dy \\ &= -\frac{\Delta b}{2fL_{y}} \left(\int_{0}^{l} \frac{h_{0}^{2}}{L_{y}^{2}} y^{2} \, dy + \int_{l}^{L_{y}} H^{2} \, dy \right) \\ &= -\frac{\Delta b h_{0}^{2}}{6fL_{y}^{3}} l^{3} - \frac{\Delta b H^{2}}{2fL_{y}} (L_{y} - l), \end{split} \tag{E5}$$

where h_0 is given by Eq. (E2) and l is given by Eq. (E3).

The toy model qualitatively captures the response of the ACC transport to wind stress changes in our simulations (Fig. E1). Importantly, it reproduces the sublinear trend of the transport with wind stress in the simulations with parameterized eddies, including those that adopt a constant $\kappa_{\rm tr}^{\rm y}$. The sublinear trend appears once the ACC transport exceeds the dashed red line,

which denotes the largest ACC transport before isopycnals start to incrop $(h_0=H)$. The results show that it is primarily the incropping of isopycnals, rather than the response of mesoscale eddies, that leads to the saturating trend of the ACC transport in the coarse-resolution simulations with flat bottom and parameterized eddies. By contrast, in the high-resolution simulations, the critical value of ACC transport is never reached, indicating that little incropping occurs even at strong wind

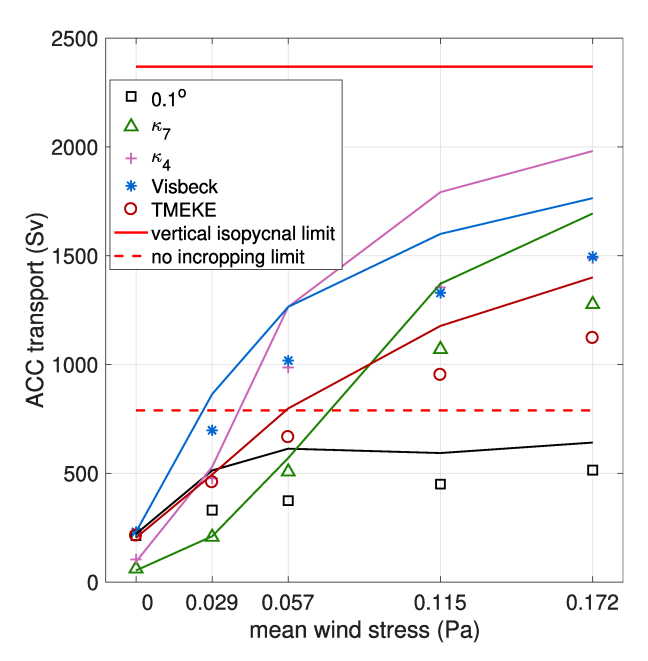


FIG. E1. The baroclinic ACC transport from the simulations (markers) and from the toy model (polylines). The toy model results are computed using Eqs. (E2), (E3), and (E5), with the diagnosed κ_{lt}^{v} from the simulations. Markers and polylines of the same color denote the same eddy parameterization. The solid red line denotes the largest possible baroclinic ACC transport, achieved when all isopycnals become vertical (i.e., $l=0, h_0 \to \infty$); the dashed red line denotes the largest possible transport without any incropping (i.e., $l=L_y, h_0=H$). Notice that the x axis here denotes the domain averaged wind stress τ , which is a more adequate measure of the effective wind stress in Eq. (E2) than the peak wind stress τ_0 .

stress, and the saturating trend of the ACC transport is indeed caused by mesoscale eddies.

REFERENCES

- Abernathey, R., and P. Cessi, 2014: Topographic enhancement of eddy efficiency in baroclinic equilibration. *J. Phys. Oceanogr.*, **44**, 2107–2126, https://doi.org/10.1175/JPO-D-14-0014.1.
- —, J. Marshall, and D. Ferreira, 2011: The dependence of Southern Ocean meridional overturning on wind stress. J. Phys. Oceanogr., 41, 2261–2278, https://doi.org/10.1175/ JPO-D-11-023.1.
- Allison, L., H. Johnson, and D. Marshall, 2011: Spin-up and adjustment of the Antarctic Circumpolar Current and global pycnocline. *J. Mar. Res.*, 69, 167–189, https://doi.org/10.1357/002224011798765330.
- Bishop, S. P., P. R. Gent, F. O. Bryan, A. F. Thompson, M. C. Long, and R. Abernathey, 2016: Southern Ocean overturning compensation in an eddy-resolving climate simulation. *J. Phys. Oceanogr.*, **46**, 1575–1592, https://doi.org/10.1175/JPO-D-15-0177.1.
- Böning, C., A. Dispert, M. Visbeck, S. Rintoul, and F. Schwarzkopf, 2008: The response of the Antarctic Circumpolar Current to recent climate change. *Nat. Geosci.*, 1, 864–869, https://doi.org/ 10.1038/ngeo362.
- Constantinou, N. C., 2018: A barotropic model of eddy saturation. J. Phys. Oceanogr., 48, 397–411, https://doi.org/10.1175/JPO-D-17-0182.1.
- ——, and A. M. Hogg, 2019: Eddy saturation of the Southern Ocean: A baroclinic versus barotropic perspective. *Geophys. Res. Lett.*, **46**, 12 202–12 212, https://doi.org/10.1029/2019GL084117.
- Eden, C., and R. J. Greatbatch, 2008: Towards a mesoscale eddy closure. *Ocean Modell.*, **20**, 223–239, https://doi.org/10.1016/j.ocemod.2007.09.002.
- Farneti, R., and P. Gent, 2011: The effects of the eddy-induced advection coefficient in a coarse-resolution coupled climate model. *Ocean Modell.*, 39, 135–145, https://doi.org/10.1016/ j.ocemod.2011.02.005.
- —, T. L. Delworth, A. J. Rosati, S. M. Griffies, and F. Zeng, 2010: The role of mesoscale eddies in the rectification of the Southern Ocean response to climate change. *J. Phys. Oceanogr.*, 40, 1539–1557, https://doi.org/10.1175/2010JPO4353.1.
- —, and Coauthors, 2015: An assessment of Antarctic Circumpolar Current and Southern Ocean meridional overturning circulation during 1958–2007 in a suite of interannual CORE-II simulations. *Ocean Modell.*, 93, 84–120, https://doi.org/10.1016/ j.ocemod.2015.07.009.
- Ferrari, R., S. M. Griffies, A. G. Nurser, and G. K. Vallis, 2010: A boundary-value problem for the parameterized mesoscale eddy transport. *Ocean Modell.*, 32, 143–156, https://doi.org/ 10.1016/j.ocemod.2010.01.004.
- Gent, P. R., and J. C. McWilliams, 1990: Isopycnal mixing in ocean circulation models. J. Phys. Oceanogr., 20, 150–155, https:// doi.org/10.1175/1520-0485(1990)020<0150:IMIOCM>2.0.CO;2.
- —, J. Willebrand, T. J. McDougall, and J. C. McWilliams, 1995: Parameterizing eddy-induced tracer transports in ocean circulation models. *J. Phys. Oceanogr.*, 25, 463–474, https://doi.org/10.1175/1520-0485(1995)025<0463:PEITTI>2.0.CO;2.
- Gnanadesikan, A., 1999: A simple predictive model for the structure of the oceanic pycnocline. *Science*, 283, 2077–2079, https://doi.org/10.1126/science.283.5410.2077.
- Hallberg, R., and A. Gnanadesikan, 2006: The role of eddies in determining the structure and response of the wind-driven

- Southern Hemisphere overturning: Results from the Modeling Eddies in the Southern Ocean (MESO) project. *J. Phys. Oceanogr.*, **36**, 2232–2252, https://doi.org/10.1175/JPO2980.1.
- Hogg, A. M., 2010: An Antarctic Circumpolar Current driven by surface buoyancy forcing. *Geophys. Res. Lett.*, 37, L23601, https://doi.org/10.1029/2010GL044777.
- Ito, T., and J. Marshall, 2008: Control of lower-limb overturning circulation in the Southern Ocean by diapycnal mixing and mesoscale eddy transfer. *J. Phys. Oceanogr.*, **38**, 2832–2845, https://doi.org/10.1175/2008JPO3878.1.
- Jansen, M. F., A. J. Adcroft, R. Hallberg, and I. M. Held, 2015: Parameterization of eddy fluxes based on a mesoscale energy budget. *Ocean Modell.*, 92, 28–41, https://doi.org/10.1016/ j.ocemod.2015.05.007.
- —, L.-P. Nadeau, and T. M. Merlis, 2018: Transient versus equilibrium response of the ocean's overturning circulation to warming. *J. Climate*, 31, 5147–5163, https://doi.org/10.1175/JCLI-D-17-0797.1.
- —, A. Adcroft, S. Khani, and H. Kong, 2019: Toward an energetically consistent, resolution aware parameterization of ocean mesoscale eddies. *J. Adv. Model. Earth Syst.*, 11, 2844–2860, https://doi.org/10.1029/2019MS001750.
- Johnson, G. C., and H. L. Bryden, 1989: On the size of the Antarctic Circumpolar Current. *Deep-Sea Res.*, 36A, 39–53, https://doi.org/10.1016/0198-0149(89)90017-4.
- Karsten, R. H., and J. Marshall, 2002: Constructing the residual circulation of the ACC from observations. *J. Phys. Oceanogr.*, 32, 3315–3327, https://doi.org/10.1175/1520-0485(2002)032<3315: CTRCOT>2.0.CO:2.
- Khani, S., M. F. Jansen, and A. Adcroft, 2019: Diagnosing subgrid mesoscale eddy fluxes with and without topography. *J. Adv. Model. Earth Syst.*, 11, 3995–4015, https://doi.org/10.1029/2019MS001721.
- Kuhlbrodt, T., R. Smith, Z. Wang, and J. Gregory, 2012: The influence of eddy parameterizations on the transport of the Antarctic Circumpolar Current in coupled climate models. *Ocean Modell.*, 52–53, 1–8, https://doi.org/10.1016/ j.ocemod.2012.04.006.
- Mak, J., J. R. Maddison, D. P. Marshall, and D. R. Munday, 2018: Implementation of a geometrically informed and energetically constrained mesoscale eddy parameterization in an ocean circulation model. *J. Phys. Oceanogr.*, 48, 2363–2382, https://doi.org/10.1175/JPO-D-18-0017.1.
- Marshall, J., and T. Radko, 2003: Residual-mean solutions for the Antarctic Circumpolar Current and its associated overturning circulation. *J. Phys. Oceanogr.*, **33**, 2341–2354, https://doi.org/10.1175/1520-0485(2003)033<2341:RSFTAC> 2.0.CO;2.
- Morrison, A. K., and A. M. Hogg, 2013: On the relationship between Southern Ocean overturning and ACC transport. *J. Phys. Oceanogr.*, **43**, 140–148, https://doi.org/10.1175/JPO-D-12-057.1.
- Munday, D. R., H. L. Johnson, and D. P. Marshall, 2013: Eddy saturation of equilibrated circumpolar currents. *J. Phys. Oceanogr.*, 43, 507–532, https://doi.org/10.1175/JPO-D-12-095.1.
- Munk, W. H., and E. Palmén, 1951: Note on the dynamics of the Antarctic Circumpolar Current. *Tellus*, 3, 53–55, https://doi.org/10.3402/tellusa.y3i1.8609.
- Nadeau, L.-P., and R. Ferrari, 2015: The role of closed gyres in setting the zonal transport of the Antarctic Circumpolar Current. J. Phys. Oceanogr., 45, 1491–1509, https://doi.org/ 10.1175/JPO-D-14-0173.1.
- —, D. N. Straub, and D. M. Holland, 2013: Comparing idealized and complex topographies in quasigeostrophic simulations of

- an Antarctic Circumpolar Current. *J. Phys. Oceanogr.*, **43**, 1821–1837, https://doi.org/10.1175/JPO-D-12-0142.1.
- Nakamura, N., 1996: Two-dimensional mixing, edge formation, and permeability diagnosed in an area coordinate. *J. Atmos. Sci.*, **53**, 1524–1537, https://doi.org/10.1175/1520-0469(1996) 053<1524:TDMEFA>2.0.CO;2.
- ——, 2001: A new look at eddy diffusivity as a mixing diagnostic. J. Atmos. Sci., 58, 3685–3701, https://doi.org/10.1175/1520-0469(2001)058<3685:ANLAED>2.0.CO;2.
- —, and D. Zhu, 2010: Finite-amplitude wave activity and diffusive flux of potential vorticity in eddy-mean flow interaction. *J. Atmos. Sci.*, 67, 2701–2716, https://doi.org/ 10.1175/2010JAS3432.1.
- Nikurashin, M., and G. Vallis, 2012: A theory of the interhemispheric meridional overturning circulation and associated stratification. *J. Phys. Oceanogr.*, 42, 1652–1667, https://doi.org/10.1175/JPO-D-11-0189.1.
- Plumb, R. A., and R. Ferrari, 2005: Transformed Eulerian-mean theory. Part I: Nonquasigeostrophic theory for eddies on a zonal-mean flow. *J. Phys. Oceanogr.*, 35, 165–174, https:// doi.org/10.1175/JPO-2669.1.
- Poulsen, M. B., M. Jochum, and R. Nuterman, 2018: Parameterized and resolved Southern Ocean eddy compensation. *Ocean Modell.*, 124, 1–15, https://doi.org/10.1016/j.ocemod.2018.01.008.
- Rintoul, S. R., and A. C. Naveira Garabato, 2013: Dynamics of the Southern Ocean Circulation. *Ocean Circulation and Climate*, G. Siedler et al., Eds., International Geophysics, Vol. 103, Academic Press, 471–492, https://doi.org/10.1016/ B978-0-12-391851-2.00018-0.

- Sinha, A., and R. P. Abernathey, 2016: Time scales of Southern Ocean eddy equilibration. *J. Phys. Oceanogr.*, **46**, 2785–2805, https://doi.org/10.1175/JPO-D-16-0041.1.
- Straub, D. N., 1993: On the transport and angular momentum balance of channel models of the Antarctic Circumpolar Current. *J. Phys. Oceanogr.*, **23**, 776–782, https://doi.org/10.1175/1520-0485(1993)023<0776:OTTAAM>2.0.CO;2.
- Swart, N. C., and J. C. Fyfe, 2012: Observed and simulated changes in the Southern Hemisphere surface westerly wind-stress. *Geophys. Res. Lett.*, 39, L16711, https://doi.org/10.1029/2012GL052810.
- Thompson, A. F., and A. C. Naveira Garabato, 2014: Equilibration of the Antarctic Circumpolar Current by standing meanders. *J. Phys. Oceanogr.*, 44, 1811–1828, https://doi.org/10.1175/ JPO-D-13-0163.1.
- Vallis, G. K., 2006: Atmospheric and Oceanic Fluid Dynamics. Cambridge University Press, 745 pp.
- Viebahn, J., and C. Eden, 2010: Towards the impact of eddies on the response of the Southern Ocean to climate change. *Ocean Modell.*, 34, 150–165, https://doi.org/10.1016/j.ocemod.2010.05.005.
- Visbeck, M., J. Marshall, T. Haine, and M. Spall, 1997: Specification of eddy transfer coefficients in coarse-resolution ocean circulation models. J. Phys. Oceanogr., 27, 381–402, https://doi.org/ 10.1175/1520-0485(1997)027<0381:SOETCI>2.0.CO;2.
- Wang, J., M. R. Mazloff, and S. T. Gille, 2016: The effect of the Kerguelen Plateau on the ocean circulation. *J. Phys. Oceanogr.*, 46, 3385–3396, https://doi.org/10.1175/JPO-D-15-0216.1.
- Young, W. R., 2012: An exact thickness-weighted average formulation of the Boussinesq equations. *J. Phys. Oceanogr.*, **42**, 692–707, https://doi.org/10.1175/JPO-D-11-0102.1.